1 The Permian-Triassic transition in the Blue Nile Basin: insights from
2 petrography and geochemistry of sandstones

3 Maryam Mansouri [1], Laura Stutenbecker [1], Matthias Hinderer [1], Anna Lewin[1], Enkurie L. Dawit[2]

4 [1] Institut für Angewandte Geowissenschaften, Technische Universität Darmstadt, Darmstadt, 64287, Germany
5 [2] Department of Geology, University of Gondar, Gondar, PO Box 196, Ethiopia

6 *Correspondence to*: Maryam Mansouri (mansouri@geo.tu-darmstadt.de)

7 **Abstract.** The Permian-Triassic transition was a time of climatic, tectonic as well as ecologic reorganizations at a global scale.
8 Clastic sedimentary successions are a key archive to study the response of earth surface processes to such extensive disruptions
9 on land. Here, we focus on the so-called Fincha Sandstone, a Karoo-equivalent fluvio- to lacustrine succession of Permian to
10 Triassic age, deposited in the Blue Nile Basin of central Ethiopia. We use thin-section petrography, bulk-rock geochemistry,
11 and heavy mineral spectra in order to decipher source rocks, as well as the possible contribution of chemical weathering and
12 recycling. The results show distinct difference between Early Permian and Late Permian to Late Triassic sandstones.
13 Petrographically, the Early Permian sandstones are rich in feldspar, and unstable heavy minerals like apatite and garnet. The
14 average chemical index of alteration, trace, and rare earth element concentrations suggest little chemical weathering and
15 relative proximity to the source area. This was controlled by a high topography, alluvial and braided systems and a semiarid
16 climate.

17 In contrast, the Late Permian and Late Triassic sandstones are quartzose, have a lower content of feldspar, and show ultra-
18 stable heavy mineral assemblages rich in zircon, rutile, and tourmaline. The chemical index of alteration is around 80 to 90 %.
19 This can be explained by a combination of recycling of mature platform sediments together with a humid climate reflected in
20 deltaic-lacustrine deposits. Most probably, a corrosive environment around the Permian-Triassic Boundary has further fostered
21 high sediment maturity.

22 In the Middle to Late Triassic, sandstones become gradually immature again, marked by a significant increase in lithoclasts
23 and metamorphic heavy minerals such as garnet. This trend is less visible in geochemical data because lithoclasts are fine-
24 grained quartzose and derive from low metamorphic terrains typical for the basement of the Arabian Nubian Shield. This
25 makes the onset of axial, NW-SE directed sediment transport through the Blue Nile Rift Basin most probable.

26 1 Introduction

27 The collision of three continental masses known as Gondwana, Laurasia, and Siberia, created the supercontinent Pangea during
28 the Permian period (McElhinny et al., 1981). Our planet has experienced dramatic climatic and ecologic disruptions during
29 this time, culminating in the most extensive mass extinction recorded in the history of life at the Permian-Triassic Boundary
30 (PTB) (Benton, 2003). The PTB is known informally as the Great Dying in which up to 96 % (Benton, 2003) of all marine

31 species and 70 % (Erwin, 1994) of terrestrial vertebrate species got extinct. Only plants and insects seem to have been less

32 affected except for a loss of ecological diversity. At the same time as this huge biological extinction, the geochemical

33 composition of the atmosphere and the oceans changed severely. The stomatal index of leaf points to much elevated CO_2 level

34 of the atmosphere and global models suggest an increase of global temperatures by 5-10 °C elevated as well as a drop of the

35 oxygen content from ca. 30 % to 16 % (Korte et al., 2003; Sun et al., 2012; Benton and Newell, 2014). Extensive marine

36 anoxia and a negative $\delta^{13}C$ excursion reflect disruption of the carbon cycle. This ecological and climate crisis is

37 contemporaneous to the outburst of continental flood basalt in Siberia (Siberian Traps). Most authors agree that the extensive

38 trap volcanism plays a major role and may have initiated a cascade of climatic and ecological changes up to the collapse of

39 entire life systems, e.g. shallow marine reef communities (Erwin, 2006). Other causes in discussion, such as asteroid impact

40 or supernova explosion, remain purely speculative. However, the exact causes of this event have not been fully understood

41 yet, although a wealth of literature exists and many stratigraphic sections have been studied in detail all over the world. Most

42 of these sections expose marine deposits including the PT stratotype at Meishan (Zheng, 2013). Continental settings are often

43 discontinuous or the exact position of the PTB is uncertain because of lacking biostratigraphic evidence (Kozur and Weems,

44 2010; Fielding et al., 2020).

45 Among continental locations, the horn of Africa hosts one of the promising sections of the Palaeozoic-Mesozoic transition in

46 the Blue Nile Basin of central Ethiopia (Dawit, 2014). This area provides one of the best examples for preserving Palaeozoic-

47 Mesozoic sedimentary rocks in eastern Africa (Dawit, 2014).

48 The area of present-day Ethiopia has been affected by three main tectonic phases including the Precambrian orogenic phase,

49 the Carboniferous-Triassic Karoo-, and the Cretaceous-Cenozoic rifting events (Wolela, 2008). Eastern Gondwana break-up

50 started during the Carboniferous-Permian time, marked by the Karoo rifting phase in Ethiopia and throughout Eastern and

51 Southern Africa (Worku, 1992). Afterward, the Late Palaeozoic-Cretaceous extensional movements in Gondwana caused the

52 formation of the Blue Nile Basin and the configuration of the basin in Ethiopia was completed by deposition of the Late

53 Palaeozoic-Mesozoic sediments under NW-SE trending rifts (Gani, 2009; Wolela, 2008; McHargue et al., 1992).

54 After two main glacial periods that affected northern Africa during the Late Ordovician-Early Silurian and Early

55 Carboniferous-Early Permian, the climate shifted from cool and temperate climate condition in the Early Permian to seasonally

56 drier conditions of the Late Permian to Middle Triassic and returned to more humid conditions during the Middle to Late

57 Triassic (Dawit, 2014; Rees, 2002).

58 The presence of 450 m thick, mostly clastic sedimentary rocks spanning from the Palaeozoic into the Mesozoic and deposited

59 under a range of climatic conditions (Jepsen and Athearn, 1964; Getaneh, 1991; Mengesha et al., 1996; Wolela, 2008), makes

60 the sedimentary fill of the Blue Nile Basin a promising continental archive to study and compare the response of earth surface

61 processes to the perturbations around the PTB. The climate warming across the PTB has been hypothesized to have caused

62 humidification and enhanced (chemical) weathering on the continents, which may have led to enhanced sediment flux and the

63 reorganization of fluvial drainage systems (Sheldon, 2006; Sephton et al., 2015; Maruoka et al., 2003; Dudas et al., 2017;

64 Mansouri and Hinderer, 2021). Also, the significant increase in the marine $^{86/87}$Sr isotope ratio during the Early Triassic is

65 commonly interpreted to reflect increasing continental erosion and weathering favored by a sparse vegetation, high

66 temperatures, acid rain and humic-poor soils (Sun et al., 2012; Benton and Newell, 2014).

67 In order to investigate these links, our approach comprises a detailed multi-proxy provenance investigation on sandstones from

68 before, around and after the PTB, and a comparison with Palaeozoic sandstones in the same area that were deposited under

69 glacial conditions with presumably less pronounced influence of chemical weathering (Lewin et al., 2018, 2020). The

70 overarching hypothesis is that changes in the continental chemical weathering rates or regime should be reflected in the

71 composition of terrestrial sandstones, e.g. through changing ratios of unstable vs. stable mineral phases. We use a combination

72 of thin section petrography, heavy mineral analysis and bulk geochemistry to better constrain the source rocks of the studied

73 sandstones, as well as potential recycling processes.

74 **2 Geological setting**

75 The tectonic evolution and geological history of Ethiopia as a part of Africa can be described in five main stages (Dawit, 2010).

76 The first stage was the collision of the Proterozoic mobile belts and the Archean cratons during the Late Neoproterozoic-Early

77 Cambrian (Pan African orogeny 900 - 550 Ma; Stern, 1994; Fig.1) and covered the whole Arabian Shield and Sahara, from

78 West Africa to the Persian Gulf and from the Mediterranean to the Sahel (Sengör et al., 2021; Unrug, 1999). The basement of

79 the Blue Nile Basin belongs to of the southern extension of the Arabian-Nubian Shield in the west (Qeissan Block) and

80 Archean-Mesoproterozoic crust in the southeast which was remobilized and incorporated into the ANS (Johnson et al., 2011).

81 As a second step, Ethiopia experienced a time of relative tectonic quiescence and associated peneplanation from the Middle

82 Cambrian until the Middle Ordovician (Dawit, 2010). After the second stage, the Ethiopian peneplain was affected severely

83 by two glacial periods in the Late Ordovician to Early Silurian ("Hirnantian ice house") and the Late Carboniferous to Early

84 Permian (Kumpulainen, 2007; Bussert, 2010; Lewin et al., 2018; 2020). In this time, the breakup of Pangea started and lasted

85 until the Late Cretaceous, resulting in the formation of several intercontinental rifts in the region (Fairbridge, 1982; Wopfner,

86 1994). The tectonic evolution of Ethiopia was completed with Cenozoic updoming and formation of the Main Ethiopian Rift

87 as earliest part of the East African Graben System (Chorowicz, 2005). This rifting was accompanied by an Early-Late

88 Oligocene volcanic event with an extrusion of 500-2000 m thick volcanic flood basalts, followed by a second event in the

89 Quaternary with up to 300 m thick volcanic rocks. These volcanic episodes are linked to the Ethiopian plateau mantle hotspot

90 (Hofmann et al., 1997, George et al., 1998, Gani et al., 2009).

91 In the Ethiopian plateau, the Blue Nile Basin is one of the main important basins which is located between latitudes of $08^0\,45^{\text{.}}$-

92 $10^0\,30^{\text{.}}$ North and longitudes of $36^0\,30^{\text{.}}$- $39^0\,00^{\text{.}}$ East (Fig. 2A). This basin covers an area of 120 000 km^2 in the central western

93 part of the region (Wolela, 1997, 2008; Russo et al., 1994; Dawit, 2010). Unfortunately, there is little literature about the

94 stratigraphy, architecture, and structural evolution of the Blue Nile basin. The reason is the extensive coverage by Cenozoic

95 volcanic rocks, which overlay the older strata and cause difficulties for subsurface investigations (Kieffer et al., 2004; Gani,

Earth **Surface**
Dynamics
Discussions

96 2009; Hofmann et al., 1997). However, in the Ethiopian plateau, the Blue Nile River has formed a ~1600 m deep gorge,

97 exposing the underlaying Late Palaeozoic-Triassic rocks (Mengesha et al., 1996; Gani et al., 2009).

98
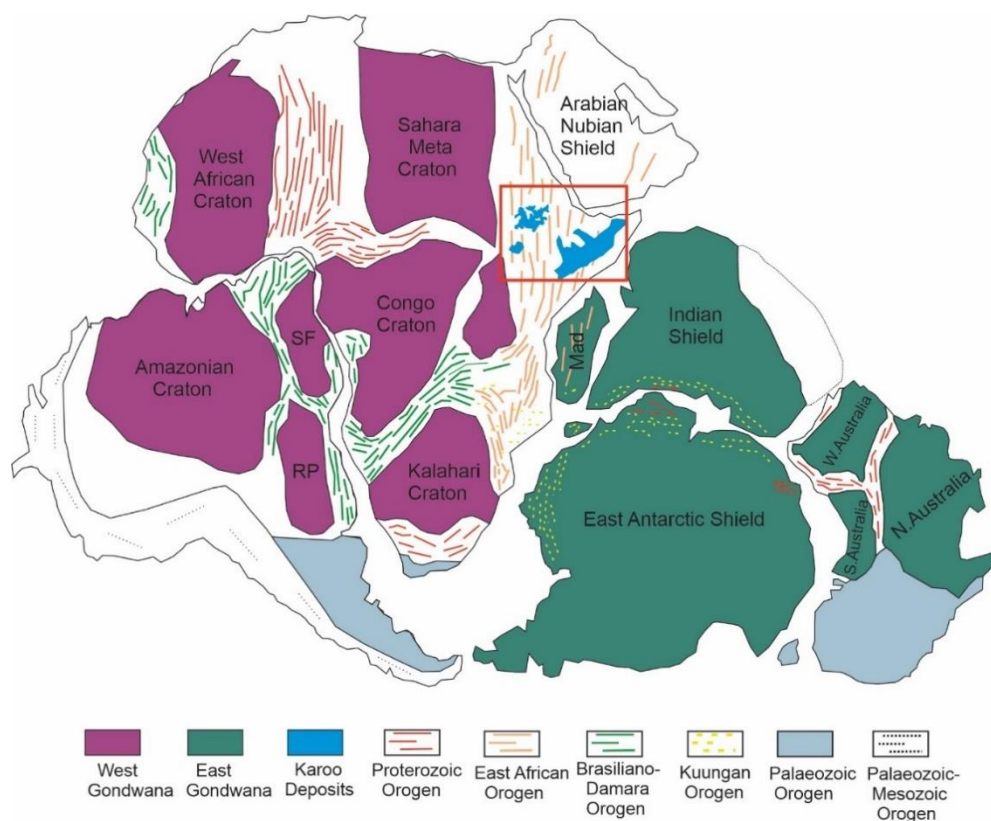
99 **Figure. 1:** Paleogeographic reconstruction of Gondwana during the Early Permian with the location of Karoo deposits in Ethiopia after
100 (Wopfner, 2009b).

101 Previous investigations reveal that the Blue Nile Basin is the result of the first phase of Karoo rifting in Permo-Carboniferous

102 times and has experienced different tectonic phases and structural complexities (Wolela, 1997, 2008; Russo et al., 1994). The

103 NE-SW direction extensional movement associated with the break-up of Gondwana (Worku and Astin, 1992; Salman and

104 Abdula, 1995; Wolela, 1997; Cannon et al., 1981) formed the NNE trending faults which can be linked to the Karoo phase

105 from Late Paleozoic to Jurassic (Gani et al., 2009). The NNE- SSW trending faults follow the Neoproterozoic basement

106 regional fabric (Gani et al., 2009). The initiation of the break-up of Gondwana caused the formation of the Blue Nile Basin

107 within NW-trending faults that controlled the rift basin in the central and eastern part of Africa (Gani et al., 2009). Morley et

108 al. (1999) proposed that the Karoo rifts have been created following former zones of weakness in the basement and have been

109 opened by oblique shear zones. The second phase of Karoo rifting happened in the Early to Middle Jurassic and caused

110 decomposition of Gondwana into separate blocks (Wolela, 2008).

111 The two recorded glacial periods in Ethiopia caused deposition of the mainly Ordovician Enticho Sandstone and the Permo-

112 Carboniferous Edaga Arbi Glacials that lay unconformably and discontinuously on the Precambrian basement (Bussert and
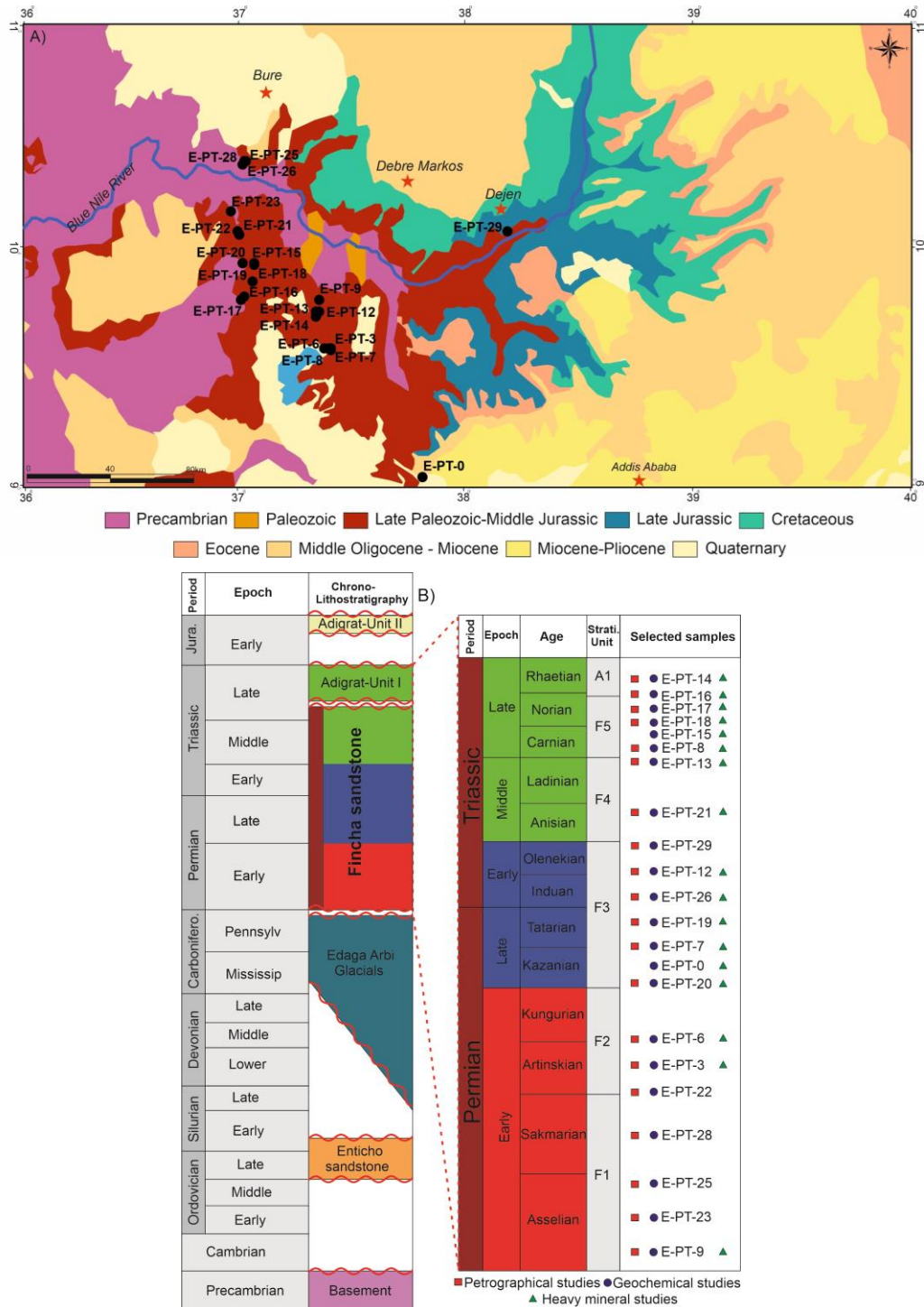
113
Figure. 2: A) The geological map of the Blue Nile region in Central Ethiopia with the sampling locations (based on geological map of
Ethiopia 2nd edition and modified after Dawit, 2010). **B)** The stratigraphic order of the Blue Nile Basin in central Ethiopia with the sample
names and related analysis. The stratigraphic units are based on Dawit, 2014.

117 Schrank, 2007; Bussert, 2010). The Precambrian basement of central Ethiopia represents the interface between the low-grade

118 metamorphic Arabian-Nubian shield in the north and the high-grade metamorphic Mozambique Belt in the south (Wolela,

119 2008; Stern et al., 2012) and is made up of granites, granodiorite, quartzites, gneisses, diorite, metasedimentary rocks,

120 hornblende-biotite gneisses, and metavolcanics (Wolela, 2008; Kazmin, 1975). Following the Permo-Carboniferous glaciation,

121 the Blue Nile Basin was filled by Karoo-equivalent deposits which covered the Edaga Arbi Glacials unconformably (Fig. 2B).

122 These mostly siliciclastic deposits are a valuable sedimentary archive recording tectonic events and climate conditions during

123 the maximum size of Pangea extension (Wopfner, 2002). The term Karoo first originated from the Great Karoo Basin which

124 is located in South Africa and contains Late Carboniferous to Early Jurassic deposits (SACS, 1980; Wopfner, 2002). Time

125 equivalent successions similar to these Karoo deposits have been reported throughout Gondwana (Wopfner, 1999; 2002;

126 Wopfner and Casshyap, 1997; Veevers and Powell, 1994; Mayne, 1971; Flores, 1973; Cannon et al., 1981). Several researches

127 have assigned different ages from Late Carboniferous to Mesozoic for them (Jespen and Athearn, 1961; Kazmin, 1975; Gani,

128 2009). From a geographical point of view, in the Early Permian, central Ethiopia moved away from the south pole further to

129 48^0 S and reached 36^0 S in the Late Permian and was located around 20^0 S of the equator during the deposition of Karoo

130 sediments (Scotese et al., 1999; Dawit, 2014).

131 Climate reconstructions of central Ethiopia based on palynological investigation indicate that warm and cool temperate climate

132 was dominating during the Late Carboniferous-Early Permian. However, micro-floral changes point towards drier seasonal

133 conditions in the Late Permian to Middle Triassic with a shift to a more humid environment in Middle to Late Triassic times

134 (Dawit, 2014).

135 The exact stratigraphic position of the Permian-Triassic successions in the Blue Nile Basin is poorly known, because of the

136 scarcity of detailed biostratigraphic evidence. Dawit (2014) presented a new lithostratigraphic and biostratigraphic framework

137 for the Permo-Triassic deposits in the Blue Nile Basin and termed them "Fincha Sandstone", equivalent to the "Karoo" or

138 "Pre-Adigrat III" deposits. He proposed five lithostratigraphic units, F1-F5, based on six informal palynological assemblage

139 zones from the Early Permian to Late Triassic (Fig. 2B). These sediments have been deposited in alluvial, meandering river,

140 and lacustrine sedimentary environments (Wolela, 2008). In this paper, we follow the stratigraphy of Dawit (2014).

141 **3 Samples and analytical methods**

142 In total, twenty-two sandstone samples have been collected from different locations in the Blue Nile Basin with focus on the

143 fine to medium sand grain sizes. Sampling sites (Fig. 2B) were selected based on the biostratigraphical and sedimentological

144 data of Dawit (2014) and Bussert (2009). In particular, the 400 m thick, well exposed and biostratigraphically relatively well

145 constrained Fincha section (Dawit, 2014) has been sampled intensively along the Blue Nile gorge (eight samples E-PT-0 to E-

146 PT-14). To guarantee a regional coverage over the central Blue Nile Basin, further fourteen samples were taken north and

147 south of the Blue Nile gorge over an area of ca. 25 000 km^2. These sampling sites were lithostratigraphically correlated by

148 considering sedimentological properties of the five units at the Fincha section described in Dawit (2014) and a thickness control

149   by taking GPS measurements of the elevation above the local basement. The latter is well visible in the field by morphological

150   and weathering features. Sampling locations and their geographic coordinates are illustrated in Fig. 2A and Table.1.

151   **Table. 1:** Sample, formation, corresponding age, stratigraphic subunit, geographical location and lithology. The stratigraphic subunit and
152   defined age are based on palynological study of Dawit, 2014.

#	Sample	Formation	Stratigraphic subunit	Age	North (^{0})	East (^{0})	Lithology
1	E-PT-14	Fincha	F5	Late Triassic	9.42236	037.20077	Sandstone
2	E-PT-16	Fincha	F5	Late Triassic	9.46330	037.00308	Sandstone
3	E-PT-17	Fincha	F5	Late Triassic	9.47415	037.00953	Sandstone
4	E-PT-18	Fincha	F5	Late Triassic	9.51388	037.03138	Sandstone
5	E-PT-15	Fincha	F5	Late Triassic	9.56154	037.00654	Sandstone
6	E-PT-8	Fincha	F5	Late Triassic	9.33749	037.22616	Sandstone
7	E-PT-13	Fincha	F4	Middle Triassic	9.43309	037.20374	Sandstone
8	E-PT-21	Fincha	F4	Middle Triassic	10.03548	036.59660	Sandstone
9	E-PT-29	Fincha	F3	Early Triassic	10.04711	038.11553	Sandstone
10	E-PT-12	Fincha	F3	Early Triassic	9.43303	037.21206	Sandstone
11	E-PT-26	Fincha	F3	Early Triassic	10.23063	37.01675	Sandstone
12	E-PT-19	Fincha	F3	Late Permian	9.55657	037.03554	Sandstone
13	E-PT-0	Fincha	F3	Late Permian	8.59685	037.49039	Sandstone
14	E-PT-7	Fincha	F3	Late Permian	9.46642	037.23712	Sandstone
15	E-PT-20	Fincha	F3	Late Permian	9.55984	037.03484	Sandstone
16	E-PT-6	Fincha	F2	Early Permian	9.33534	037.24334	Sandstone
17	E-PT-3	Fincha	F2	Late Permian	9.33348	037.24341	Sandstone
18	E-PT-28	Fincha	F1	Early Permian	10.23206	037.00941	Sandstone
19	E-PT-25	Fincha	F1	Early Permian	10.22231	037.00627	Sandstone
20	E-PT-23	Fincha	F1	Early Permian	10.09648	036.57534	Sandstone
21	E-PT-22	Fincha	F1	Early Permian	10.04305	036.59317	Sandstone
22	E-PT-9	Fincha	F1	Early Permian	9.46642	037.2101	Sandstone

153   Due to the aim of our study we selected and categorised our samples into Early Permian, Late Permian to Early Triassic, and

154   Middle to Late Triassic. Accordingly, seven samples were collected from defined stratigraphic units F1 to F2 that are assigned

155   to Early Permian, seven samples from unit F3 or Late Permian to Early Triassic and eight samples from units F4-F5 or the

156   Middle to Late Triassic period. In order to test potential recycling of older sedimentary rocks, we have used compositional

157   data from the Enticho and Edaga Arbi glacials as a comparison from the work of Lewin et al. (2018, 2020).

158   **3.1 Petrography**

159   Petrographic studies were carried out under the polarization microscope on 20 prepared thin sections to constrain the sandstone

160   framework composition (summary see Table 2). For each sample, 300 grains were point-counted using the Gazzi-Dickinson

161   method (Dickinson, 1970; Ingersoll et al., 1984). The counting was done with a Pelcon automated point-counter that moves

162 along a grid of equally-spaced points (Glagolev-Chayes method, Galehouse, 1971). The Folk (1968) ternary plot was used to

163 illustrate the sandstone framework composition. The degree of roundness and sorting of the sandstone framework were

164 estimated using the scale of Powers (1953).

3.2 Geochemistry

166 About 50 g of each sandstone sample was pulverised by using a vibratory disc mill equipped with agate vessels for 10 min to

167 obtain a particle size of <63 µm. Major oxides and trace elements concentrations were determined by X-ray fluorescence

168 spectrometry on fusion tablets at the Geoscience center of Göttingen university and Technical University of Darmstadt.

169 The rare earth element (REE) concentrations were determined using an Analytik Jena Plasma Quant MS Elite® inductively

170 coupled plasma mass spectrometer (ICP-MS) at the Technical University of Darmstadt. To prepare samples for ICP-MS

171 measurement, the decomposition of dry and homogenized samples was performed by lithium metaborate fusion using a

172 Katanax® X300 fluxer. For each sample about 0.2 g of powdered material was mixed with 2 g of lithium borate flux agent in

173 a platinum crucible. The mixed sample was fused for 10 minutes at 1000°C. The molten flux was dissolved automatically in

174 80 ml of 5% nitric acid (HNO_3). The dissolved sample was transferred to the measuring flask and was filled up with the

175 dissolved materials to 100 ml. The prepared samples were diluted 20 fold before ICP-MS measurement.

176 Trace elements were normalised to the upper continental crust (UCC; Taylor and McLennan, 2009; McLennan, 2001) and

177 REE to chondrites (Taylor and McLennan, 1985). To calculate the Eu anomaly, we have used the McLennan equation (1989)

178 as follow:

179 $$\frac{Eu}{Eu^*} = \frac{Eu_N}{(Sm_N \times Gd_N)^{0.5}}$$

180 in which the chondrite normalised value is shown by subscript N.

181 To evaluate the degree of paleo-weathering of sandstones, the chemical index of alteration (CIA of Nesbitt and Young, 1982)

182 and weathering index of Parker (WIP of Parker, 1970) have been used as follow:

183 CIA= [Al2O3) / (Al2O3 + CaO* + Na2O + K2O] × 100

184 WIP = [((Ca) / 0.7) + (2 Na / 0.35) + (2 K / 0.25) + (Mg / 0.9)] × 100

185 CaO* presents the Ca of silicates only and has been corrected for the carbonate-bearing samples.

3.3 Heavy minerals

187 Based on different stratigraphy order, petrography and geochemical compositions, 17 samples were chosen for heavy mineral

188 analysis. About 500 g of each sample was disaggregated very carefully by mortar and pestle to avoid the artificial crushing of

189 grains. Then the material was separated by wet-sieving with a mechanical shaker to get <63 µm, 63-125 µm, 125-250 µm, and

190 250-500 µm grain size fractions. In order to achieve comparability with previous studies on the older strata in the Blue Nile

191 basin (Lewin et al., 2020), we selected the 63-125 µm fraction for the analysis. The selected samples were treated with acetic

192 acid (10 %) and Na-dithionite solution (Andò, 2020) to remove carbonate cement and iron oxides, respectively. Afterward, we

Table. 2: Petrographical results based on the point counting analysis of the sandstones framework. Abbreviations are as follow: Stra. Subunit: Stratigraphic subunit; Qzm: monocrystalline quartz; Qzmu: monocrystalline quartz with undulose extinction; Qzp: polycrystalline quartz; Qzmicr: microcrystalline quartz; Pl: plagioclase; Kfs: potassium feldspar; Lp: plutonic lithic fragment; Lv: volcanic lithic fragment; Ls: sedimentary lithic fragments; Lm: metamorphic lithic fragment; Unid: unidentified: altered minerals; Abbreviation for accessories: Ap: apatite, Ms: muscovite, Op: opaque, St: staurolite, Tur: tourmaline, Zrn: zircon, Bi: Biotite, Ru: rutile. Abbreviation for roundness (R.): −−:angular, − : subangular, 0: subrounded, + : rounded, ++: well rounded. Abbreviation for carbonate cement (C.): 0: not present, + : up to 5 %, ++ : 20–25 %. Abbreviation for sorting: −−: very poor, − : poor, 0 : moderate, + : good, ++ : very good.

Sample name	Stra. subunit	QZm %	QZmu %	QZp %	Qzmicr %	Pl %	Kfs %	Lp %	Lv %	Ls %	Lmi %	Lu %	undi. %	Counts	Accessories	R.	GS (mm)	C.	Sorting
E-PT-14	MLT	40.7	3.7	8.7	0	0.3	0	0	0	3	43.7	0	0	300	Ru, Op, Zr	0 to +	0.02-0.03	0	0
E-PT-16	MLT	43.7	7.3	11	2.7	0	5.3	2	0	17.3	10.7	0	0	300		-	0.05-0.12	0	0 to -
E-PT-17	MLT	25.3	7.7	42	3	0	0	4.3	0	6.3	10.3	0	1	300	Op, Bt, Zr, Ru	- to 0	0.02	0	- to 0
E-PT-18	MLT	36.3	6	29	5.7	0	0	2.3	0.3	9	11.3	0	0	300	Ms, Op, Zr	-	0.1	0	0
E-PT-8	MLT	32.7	8.3	47.3	0	2.3	1	0	0	0.7	7.7	0	0	300	Ms, Op, Zr	0 to +	0.02	0	0
E-PT-13	MLT	43.7	7.3	23.3	0.7	0.3	9.7	3.3	0	6.7	3	0.7	1	300	Bt, Op, Zr	--	0.1	0	0
E-PT-21	MLT	54.3	9.7	16.7	1.7	0.3	1	0	0	5.3	10.7	0	0.3	300	Bt, Zr	-	0.07-0.1	0	0
E-PT-29	PTB	38.3	6	30.3	0.7	0.7	3.3	1	1.7	3	14.3	0.7	0	300		-	0.1-0.3	0	0
E-PT-12	PTB	83.7	8.7	7.3	0.3	0	0	0	0	0	0	0	0	300		+	0.06	0	++
E-PT-26	PTB	52.3	34	13	0	0	0	0	0	0	0	0	0.3	300		+	0.1-0.2	0	+
E-PT-19	PTB	50.8	4.8	13.7	0.0	0.0	4.8	1.0	0.0	10.2	14.9	0	0	300		-	0.01	0	0 to -
E-PT-7	PTB	58.7	10	24.7	0	3	1.7	0	0	0	2	0	0	300	Ms, Op, Zr	0	0.02	0	0
E-PT-20	PTB	62	11	3	0.3	1.3	8	0	0	11.7	0	0	0	300	Ms, Op, Tur, Zr	--	0.07-0.56	0	0 to -
E-PT-6	EP	72	5	13.3	0	7.3	1.7	0	0	0	0	2.3	0	300	Op,Ms,Zr, Ru	--	0.02	+	--
E-PT-3	EP	45.5	0.6	3.9	0.0	3.2	46.8	0	0	0	0	0	0	300		--	0.01	0	-
E-PT-22	EP	61	4.3	0.7	17.3	1.3	7.3	0	0	8	0	0	0	300	Op.Ap. , Tur, Zr, Ru	--	0.02	0	--
E-PT-28	EP	63.7	16	4.7	0	5.3	9	0.3	0	0	0	1	0	300		-	0.1-0.3	0	-
E-PT-25	EP	49.3	9.3	2	0	26	12.3	0	0	0.3	0	0.7	0	300		-	0.01	++	-
E-PT-23	EP	54	5	0	0	29.3	10.7	0	0.7	0.3	0	0	0	300	Op.Ap,Ms,Zr, Ru	-	0.1	+	- to 0
E-PT-9	EP	62	11.7	5.7	0	5.3	14.7	0.3	0	0	0	0	0	300	Ap, Ru, Ms	--	0.01	++	--

196 The obtained heavy mineral concentrates were weighed, split using a microriffle splitter and the heavy minerals were mounted

197 on strewn slides using Cargille Meltmount™ with a refraction index of 1.662. In order to identify the heavy minerals

198 assemblage, we counted around ~300 transparent grains in each sample using the polarizing microscope (Table. 3).

199 **Table. 3:** Heavy minerals percentages based on point counting analysis.

Sample	Stra. subunit	Zircon %	Rutile %	Tourmaline %	Garnet %	Apatite %	Epidote %	Staurolite %	Chloritoid %	Monazite %	Titanite %	Others %	Opaque %
E-PT-14	MLT	8.1	12.9	9.7	66.1	1.6	1.6	0.0	0.0	0.0	0.0	0.0	32
E-PT-16	MLT	19.3	22.8	11.4	30.7	0.0	7.0	1.8	1.8	0.0	5.3	0.0	65
E-PT-17	MLT	32.2	38.4	8.2	12.3	2.7	4.1	1.4	0.0	0.7	0.0	0.0	65
E-PT-18	MLT	48.8	33.0	6.7	0.3	0.0	0.0	2.6	0.0	3.2	0.0	5.3	73
E-PT-15	MLT	47.6	41.6	6.7	0.4	0.0	0.0	0.4	0.0	1.1	0.0	2.2	87
E-PT-8	MLT	21.9	31.1	42.0	0.7	1.5	0.0	1.3	1.3	0.0	0.0	0.0	48
E-PT-13	MLT	33.3	36.4	16.7	0.0	13.6	0.0	0.0	0.0	0.0	0.0	0.0	72
E-PT-21	MLT	33.5	55.8	7.6	0.0	2.2	0.0	0.0	0.0	0.0	0.9	0.0	81
E-PT-12	PTB	39.3	2.1	53.9	0.3	4.3	0.0	0.0	0.0	0.0	0.0	0.0	35
E-PT-26	PTB	53.8	20.3	20.9	0.0	0.0	0.6	0.0	0.0	0.0	0.0	4.4	72
E-PT-19	PTB	28.0	13.4	31.7	0.0	11.0	2.4	0.0	6.1	4.9	2.4	0.0	86
E-PT-0	PTB	24.0	22.8	26.2	22.8	0.4	0.0	0.0	0.0	1.9	0.0	1.9	90
E-PT-7	PTB	4.8	8.3	14.3	13.1	59.5	0.0	0.0	0.0	0.0	0.0	0.0	64
E-PT-20	PTB	1.6	1.6	15.6	7.2	60.4	0.0	1.6	0.8	0.0	11.2	0.0	86
E-PT-6	EP	24.1	0.0	6.0	67.3	2.6	0.0	0.0	0.0	0.0	0.0	0.0	61
E-PT-3	EP	2.7	7.7	1.0	71.0	17.7	0.0	0.0	0.0	0.0	0.0	0.0	64
E-PT-9	EP	10.0	3.3	3.3	21.7	61.7	0.0	0.0	0.0	0.0	0.0	0.0	68

200 **4 Results**

201 **4.1 Petrography**

202 According to the classification scheme of Folk (1968), the Early Permian samples can be classified as sub-arkose and arkose,

203 and contain on average 70 % quartz, 25 % feldspar, and 4.5 % rock fragments. The dominant rock fragments in the Early

204 Permian samples are sedimentary lithoclasts (Fig. 3). Rutile, zircon, apatite, garnet, and opaque phases are accessory minerals.

205 The Early Permian samples are rich in carbonate cement and grains are angular to subangular with very poor to poor sorting

206 (Fig. 4 and Table 2).

207 The Late Permian to Early Triassic samples show a higher amount of quartz (about 87 %), 10 % rock fragments and about 2

208 % feldspar. Three samples consist to more than 90 % of quartz and are thus categorized as quartzarenites (Fig. 3). The

209   remaining two samples have a high amount of rock fragments around 23 % and categorize as sub-litharenite to litharenite. The
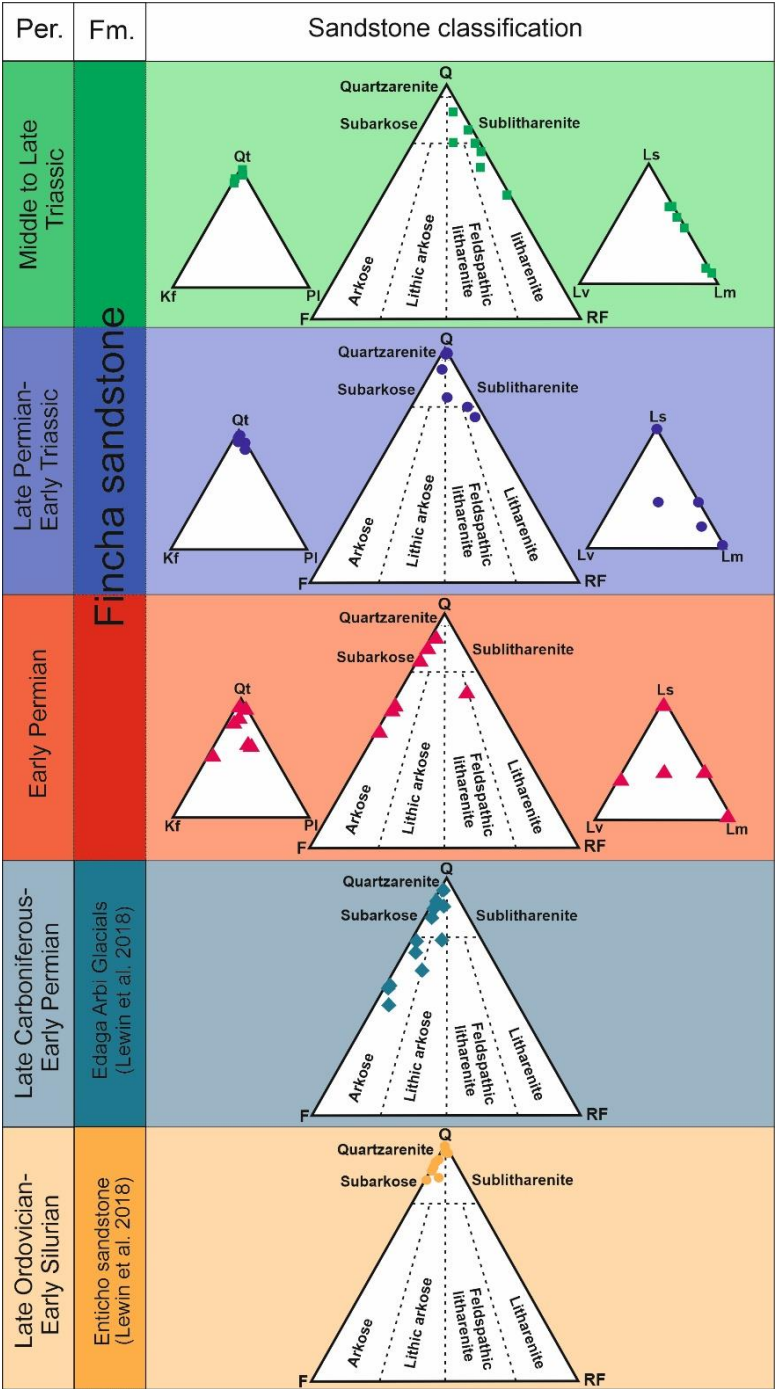
210

211   **Figure. 3:** Sandstone classification scheme of Folk, 1968 for the Edaga Arbi Glacials and Enticho sandstones (from Lewin et al., 2018),
212   Lower Permian, Late Permian to Early Triassic and Middle to Late Triassic samples (this study).

213 lithic components are of metamorphic and sedimentary origin with 15 % and 7 %, respectively. The accessory minerals are

214 zircon, tourmaline, rutile, and opaque minerals. Here, the sandstones are more heterogeneous with different degree of sorting

215 from well sorted sandstones to moderate types. The grains have angular, subangular to rounded shapes (Table. 2 and Fig. 4).
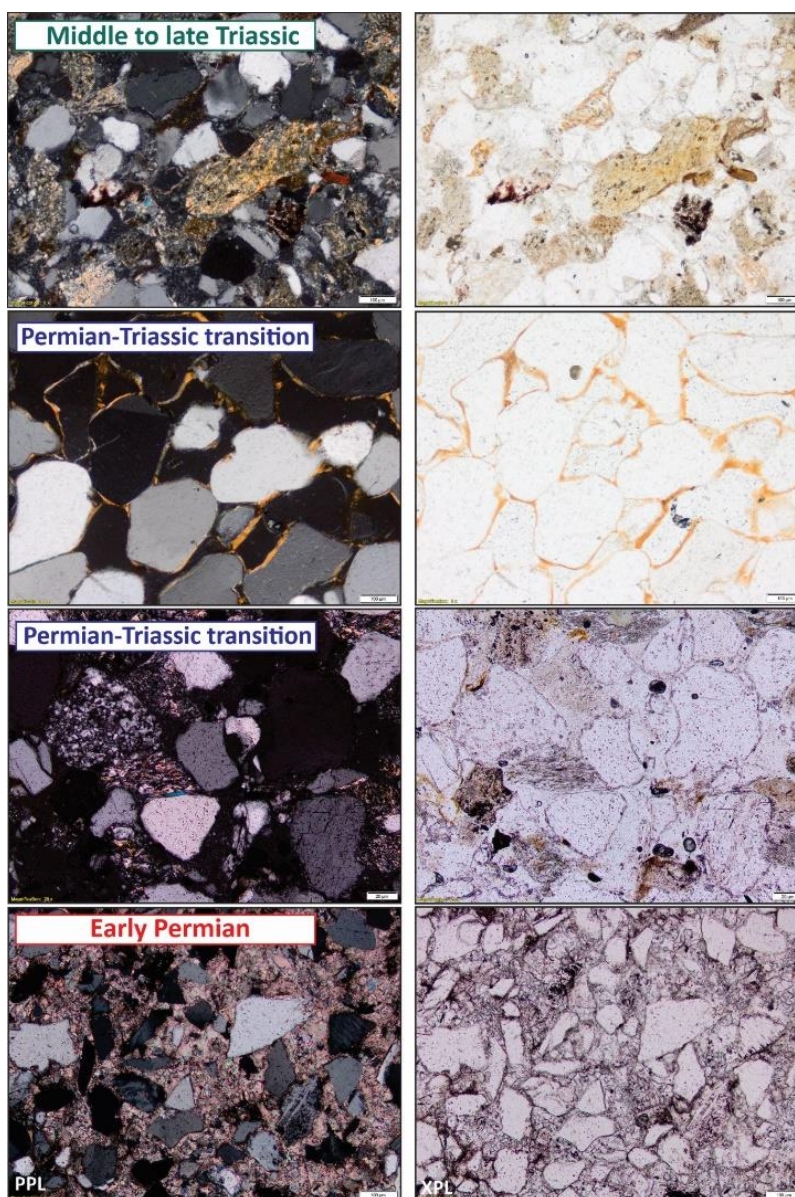
216

217 **Figure. 4:** Thin section microscopic images of the Early Permian to Late Triassic Fincha sandstone. The scale bar is 100 um.

218 By moving toward the Middle to Late Triassic, the sandstones tend to be richer in lithic fragments and are categorised as

219 litharenites and sub-litharenites (Fig. 3 and Fig.4). The averaged counted grains are about 71 % quartz, 23 % rock fragments,

220 and 3 % feldspar. In comparison to the Late Permian to Early Triassic samples, the feldspar proportion is increased with the

highest amounts in samples E-PT-13 and E-PT-16 (about 10 % and 5 %, respectively). The abundant lithic fragments are of metamorphic and sedimentary origin with the average of 14 % and 9 %, respectively. The accessory minerals are zircon, tourmaline, rutile, and opaques. Sandstones are moderately sorted, and the grains are categorised as very angular to rounded shapes (Table. 2).

4.2 Geochemistry

Major oxides have been plotted against Al_2O_3 because of the immobile behaviour of Al during weathering, diagenetic and metamorphic processes (Bauluz et al., 2000). The plotted SiO_2 against Al_2O_3 illustrate that the SiO_2 concentration is high in the Late Permian to Late Triassic samples while the Al_2O_3 and TiO_2 concentrations are higher in the Early Permian samples (Fig. 5).
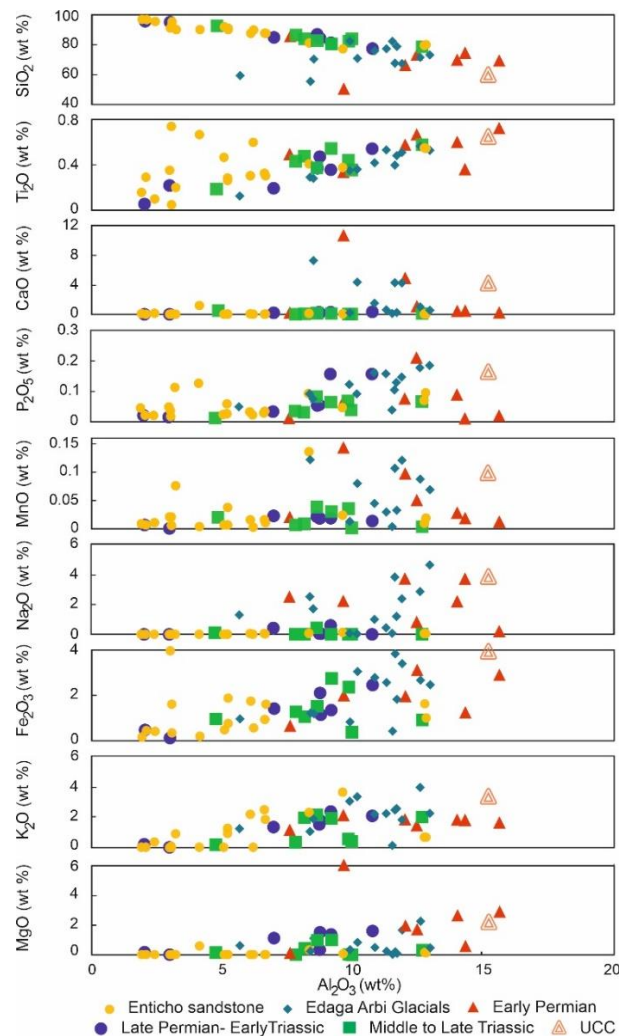
Figure. 5: Plots of the major oxides against Al_2O_3 for the analysed samples. Data for UCC (from McLennan, 2001; Taylor and McLennan, 2009).

233 CaO and MgO are low in all samples, except the Early Permian samples, which contain carbonate cement. NaO$_2$ is higher in
234 the Early Permian samples while it is very low in the other intervals. K$_2$O, Fe$_2$O$_3$, and P$_2$O$_5$ contents are variable in all studied
235 samples but they are enriched in the Early Permian samples more than others (Fig.5).

236 The results of the normalised trace elements against UCC have been summarised in spider plots in Fig. 6A. Large ion lithophile
237 elements (LILE) like Rb, Ba, and Sr are slightly depleted in the Early Permian samples, while the depletion trend is greater in
238 the Late Permian to Late Triassic samples especially in the samples E-PT-12 and E-PT-26. However, high field strength
239 elements (HFSE) such as Th, U, Y, Zr, and Nb are enriched in the Middle to Late Triassic samples compared to the Early
240 Permian and Late Permian to Early Triassic samples. Other elements such as transition metals are depleted in all intervals
241 except Sc and Cr in the Early Permian samples (Fig. 6A).
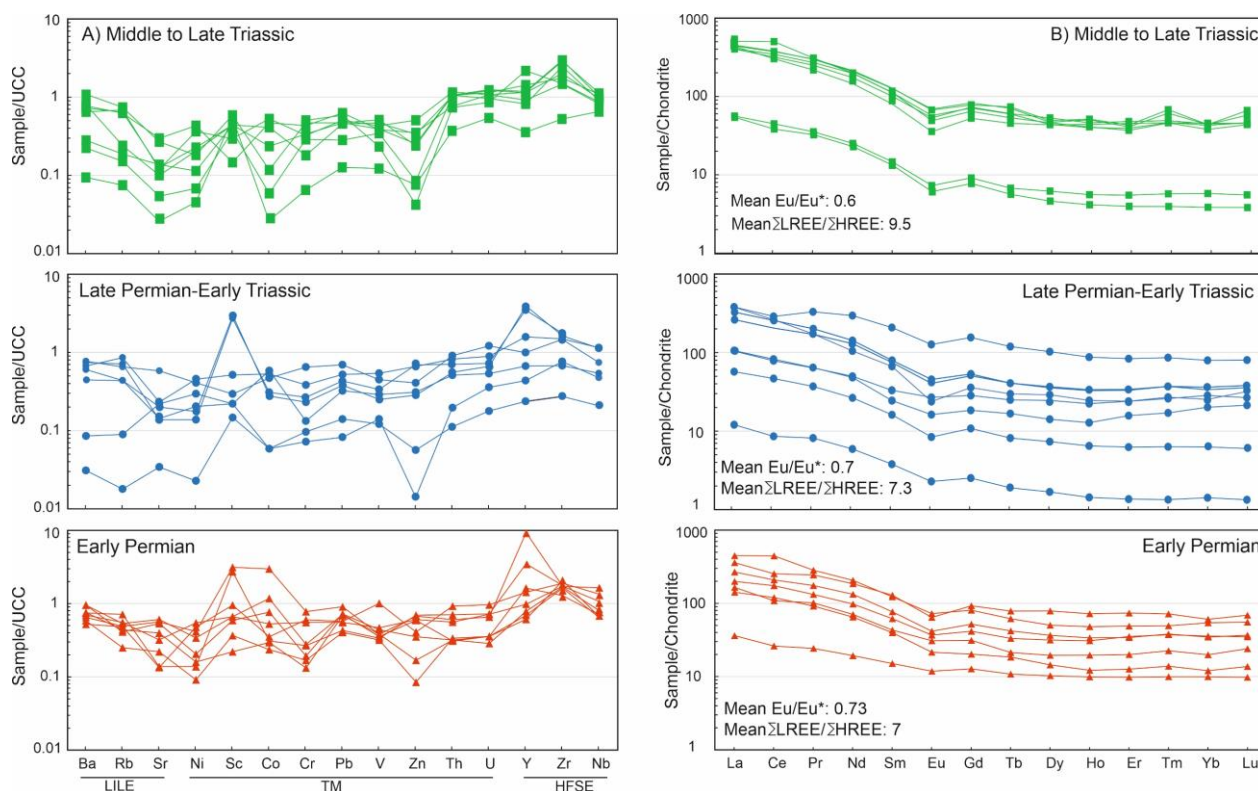
242

243 **Figure. 6: A)** Normalised trace element concentrations against UCC (from McLennan, 2001; Taylor and McLennan, 2009), LILE: Large
244 ion lithophile elements, TM: Transitional metals, HFSE: High field strength elements and **B)** Rare earth element concentrations against
245 chondrite values (from Taylor and McLennan, 1985).

246 The normalised REE against chondrite values are plotted in Fig. 6B. The Early Permian samples are enriched in the light rare
247 earth elements (LREE) with a flat trend for the heavy rare earth elements (HREE) except one sample E-PT-9, which is depleted
248 in REE compared to the others. The average chondrite-normalized La$_N$/Yb$_N$ for the Early Permian samples is about 7 with a
249 mean Eu/Eu* of 0.73, La$_N$/Sm$_N$ 3.2, and Gd$_N$/Yb$_N$ 1.4. The mean CIA and WIP values for the Early Permian samples are about
250 59 and 47, respectively (Fig. 7A).

251 The REE pattern in the Late Permian to Early Triassic samples is more variable and is highly depleted in the sample E-PT-12.

252 The La_N/Yb_N value in the Late Permian to Early Triassic samples is on average 8 with an Eu anomaly of 0.7, La_N/Sm_N of 3.6

253 and Gd_N/Yb_N of 1.5. The CIA value is high for the Late Permian to Early Triassic samples, about 82, while the WIP value is

254 very low, about 16 (Fig. 7A).

255 The Middle to Late Triassic samples are enriched in the LREE with more pronounced negative Eu anomaly and a steeper

256 HREE trend except sample E-PT-13 and E-PT-15, which is depleted strongly in comparison to the others. The averaged

257 La_N/Sm_N and Gd_N/Yb_N are higher than UCC values, about 4.1 and 1.4, respectively, with a negative Eu anomaly of 0.6 and

258 average of La_N/Yb_N of 11. The WIP value in the Middle to Late Triassic samples is about 12, while the CIA value is 87 (Fig.

259 7A).
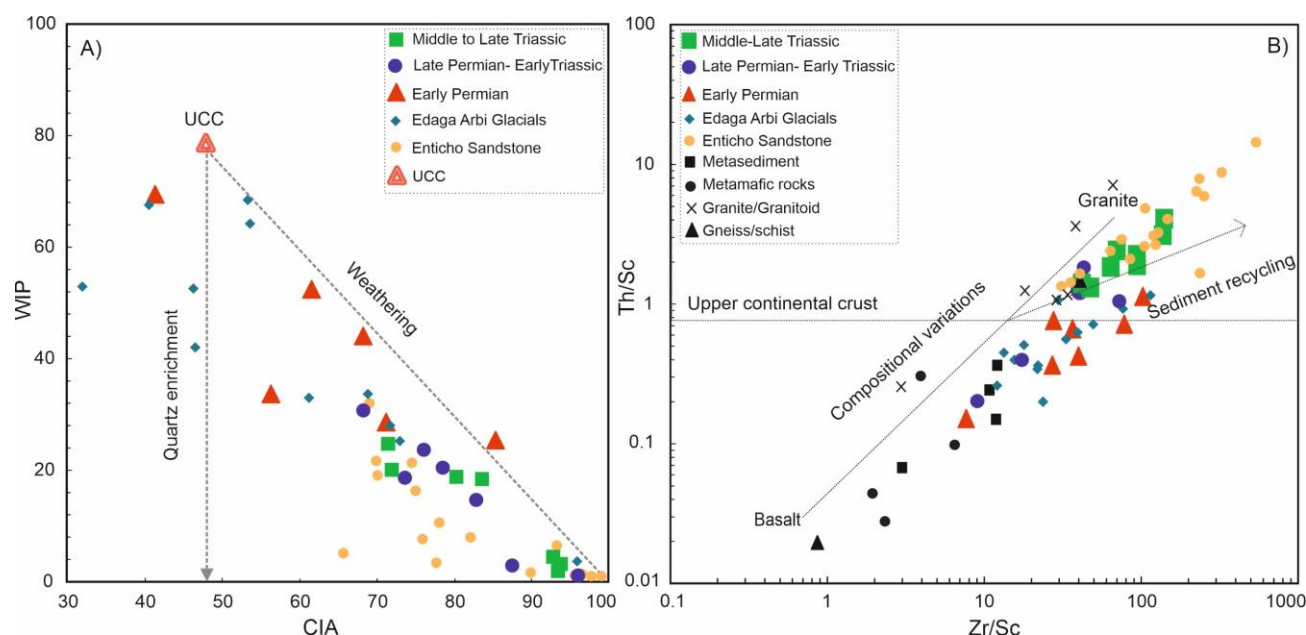
260

Figure. 7: A) Chemical index of alteration (CIA, after Nesbitt and Young, 1982), and weathering index of Parker (WIP; after Parker, 1970)
for the studied samples. **B)** Zr/Sc, and Th/Sc plot (after McLennan et al., 1993) samples of the Fincha Sandstone plotted with Enticho, Edaga
Arbi Glacials, and basement from Lewin et al., 2018.

264 The PCA biplot of the Fincha Sandstone based on centred log ratio transformation from major, trace, and rare earth elements

265 show a clear separation between Early Permian samples and Middle to Late Triassic ones, with Late Permian to Early Triassic

266 samples plotting in between (Fig. 8A). The Lower Permian samples can be distinguished from Upper Permian to Upper Triassic

267 along the arrows of Na, Ca, K, Mg, and Mn. Immobile elements show a distinct difference between them as well. Ba, Rb, and

268 Sr are positively correlated in the Early Permian samples while these elements are negatively correlated with Th, U, Zr, Si, Ti,

269 REE, Eu/Eu*, and Nb in Middle to Late Triassic and partly in the Late Permian to the Early Triassic samples. The PCA biplot

270 of Fincha Sandstone with Enticho and Edaga Arbi Glacials reveals close similarity between Early Permian samples and Edaga

271 Arbi Glacials. PC1 in Early Permian and Edaga Arbi samples show positive loading with Mg, Mn, Na, Ca, and Ba (Fig. 8B).

Earth **Surface**
Dynamics
Discussions

272 From the other side, enrichments of Enticho Sandstone and Late Permian to Late Triassic samples in REE, Fe, Ni, U, Th, Si

273 and Zr show a similar trend (Fig. 8B).

274
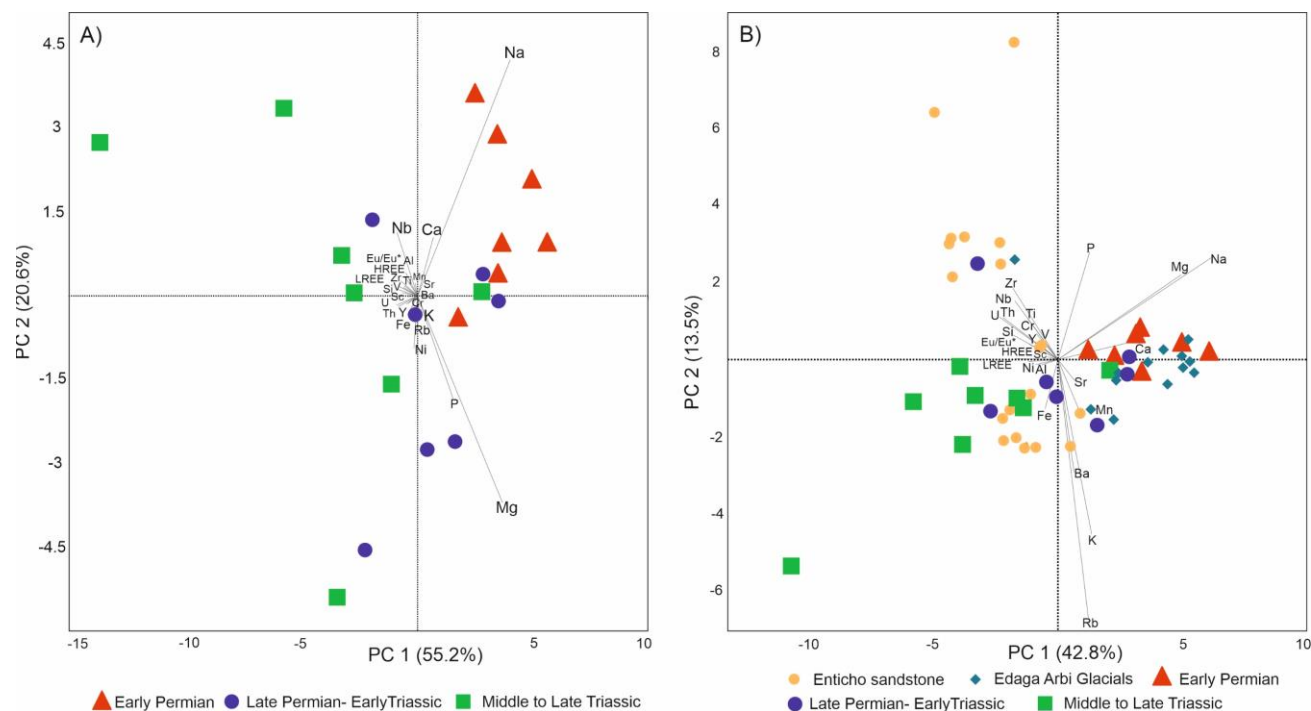
275 **Figure. 8:** Compositional biplots of the first two principle components of the principle component analysis based on the clr-transformed
276 concentration of the major, trace and rare earth elements **A)** this study **B)** Completing and comparing this study with the Enticho and Edaga
277 Arbi Glacials samples from Lewin et al., 2018.

278 **4.3 Heavy minerals analysis**

279 The heavy mineral concentration (HMC, Garzanti and Andò, 2007) is generally poor with an average of 0.93 %, but varies

280 between 1.9 % and 0.11 % with a slightly increasing concentration towards the Middle to Late Triassic samples.

281 The ratio between opaque and transparent heavy minerals is about 0.63. However, there is not an obvious or meaningful trend

282 between the ratio of transparent and opaque minerals, and they do not show any pattern in the three defined intervals. Therefore,

283 opaque and spurious minerals have been excluded from the graphs to give a clear view of the transparent heavy mineral

284 distribution.

285 The heavy minerals assemblage of the Early Permian samples is dominated by relatively unstable heavy minerals like garnet

286 and apatite with 53 % and 27 %, respectively (Figs. 9 and 10). Ultra-stable minerals like zircon, rutile, and tourmaline form

287 the rest of the heavy mineral population. The average percentage of the unstable heavy minerals are about 84 %, which prevails

288 over 19 % of the ultra-stable minerals.

289 The heavy mineral spectra of the Late Permian to Early Triassic can be subdivided into two groups. The Late Permian samples
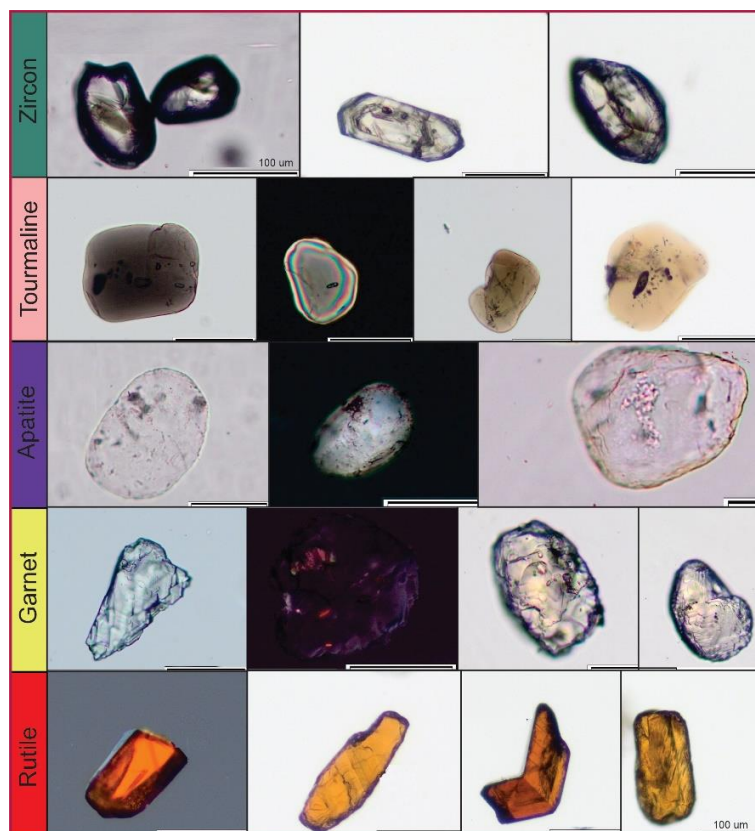
are dominated by an average of 60 % apatite, whereas the Early Triassic samples contain about 86 % ultra-stable zircon,

tourmaline, and rutile. Zircon is the most abundant heavy mineral followed by tourmaline and rutile (Figs. 9 and 10).

Figure. 9: Microscopic images of the most encountered heavy minerals in the analysed Early Permian to Late Triassic sandstone samples.

The dominance of ultra-stable heavy minerals continues into the Middle to Late Triassic, but decreases again at the top of the Triassic samples. In the Late Triassic, garnet makes up to about 66 % of the total amount. The other encountered heavy minerals are staurolite, monazite, and chloritoid.

Based on the classification schemes of Gärtner et al. (2013) and Corfu et al. (2003), the morphometry of Early Permian zircons is variable and both rounded/subrounded to angular/subangular grains occur. The zircons in the Middle to Late Triassic interval are predominantly rounded to subrounded, whereas the Late Permian to Early Triassic zircons are mostly angular to sub-angular grains (Fig. 11). The apatite grains are almost angular to sub-rounded in the Early Permian samples in comparison to the rounded and sub-rounded grains of the Late Triassic. The morphometry of apatite grains (Fig. 11) is more variable and a clear stratigraphic trend is not visible. Nevertheless, some variations are concordant for zircons and apatite, e.g. the high angularity of grains in sample E-PT-26 or E-PT-8, and the high roundness in sample E-PT-12 or E-PT-16. This points to repeated transport of both populations.

305
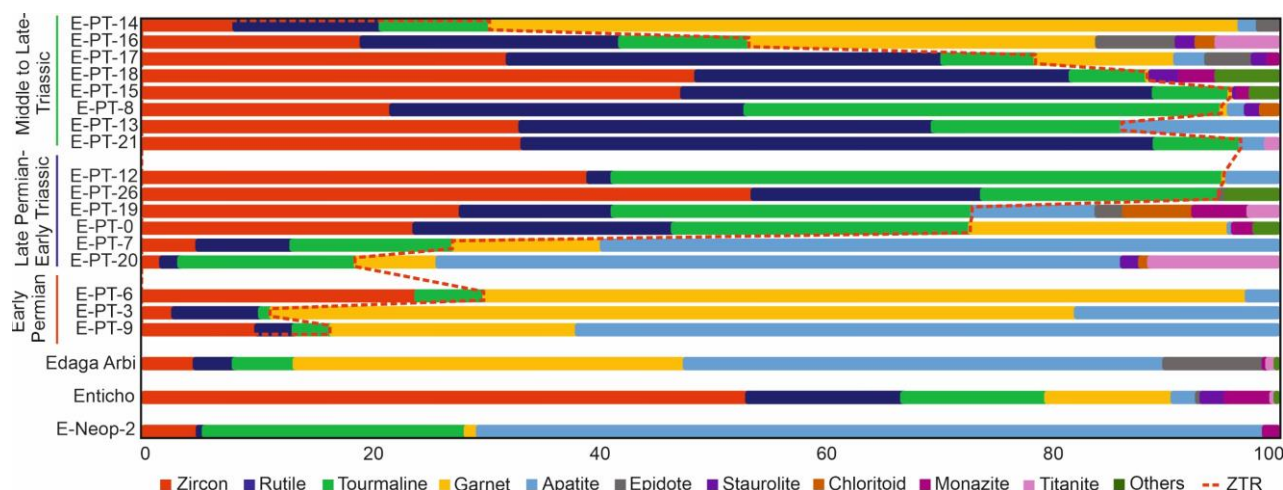
Figure. 10: Heavy mineral assemblages of the studied samples and the averaged HM spectra of the Enticho and Edaga Arbi Glacials from
(Lewin et al., 2020).

The plotted heavy mineral indices based on Morton and Hallsworth (1994) show an inverse correlation between zircon-
tourmaline-rutile index (ZTR) on the one hand and the garnet-zircon index (GZi) and apatite-tourmaline index (ATi) on the
other hand. In the Early Permian samples, the ZTR index is low, increases in the Late Permian to Triassic and drops again in
the Late Triassic samples (Table 4). The RZi is almost constant in all intervals except in the lower part of the Early Permian
and in the Early Triassic. The ATi is high in the Early Permian samples, while is very low in the Late Permian to the Triassic
samples. The GZi shows the same trend as AZi and is strongly increased in the Late Triassic samples (Fig. 11).

5 Discussion

5.1 Stratigraphic trends

The petrographic and geochemical results show clear trends of changing sandstone composition from the Early Permian to the
Late Triassic in the Blue Nile Basin. In the following we discuss arguments for changes of the source area, recycling of glacial
deposits, and climatic changes including expected extreme conditions around the PTB.

The petrographical analysis shows that the Early Permian sandstones are poorly sorted and immature with higher content of
feldspar and unstable heavy minerals. The higher content of carbonate cement, however, is of secondary origin due to
cementation of basal sandstones in the basin by diagenetic fluids. Heavy mineral spectra are dominated by garnet up to 42 %
and ultra-stable heavy minerals make up only 12 %. The petrographic signatures in the Early Permian point to short sediment
transport and/or weak chemical weathering. This is also reflected in the geochemical data, where SiO_2 is lowest and Al_2O_3
highest. The mobile trace elements LILE are less depleted than in the other intervals. Generally, Early Permian sandstones
come closest to the geochemical average of the UCC.

This contrasts to the Late Permian to Triassic sandstones which are highly quartzose and rich in ultra-stable minerals ~70 %.

Earth **Surface**
Dynamics
Discussions

327
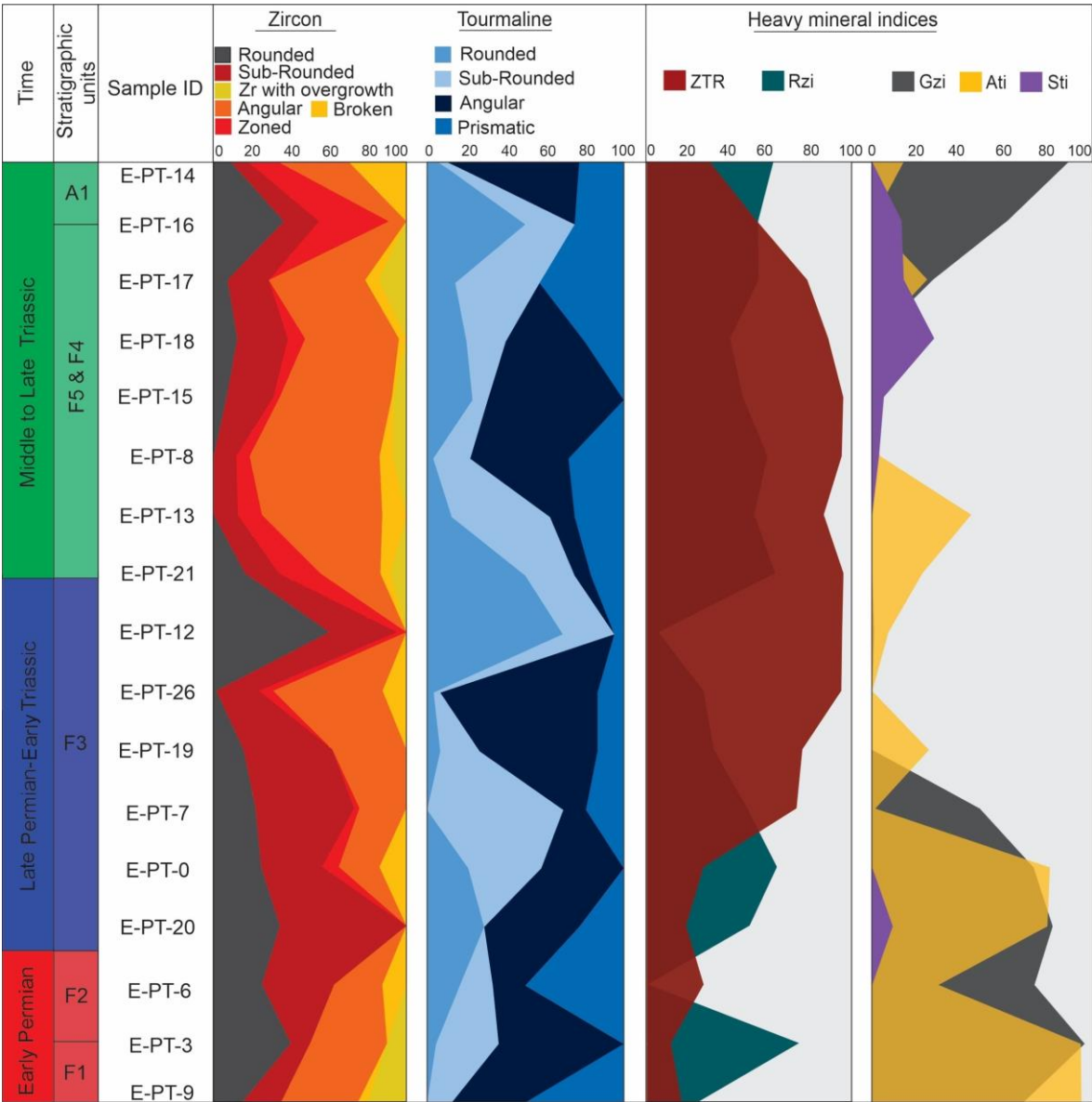
Figure. 11: Shape and roundness analysis of the zircon and tourmaline minerals with the heavy mineral indices. ZTR: Zircon-Tourmaline-Rutile index; Rzi: Rutile-zircon index; Gzi: Garnet-zircon index; Ati: Apatite-tourmaline index, Sti: Staurolite - tourmaline index.

On the other hand, a higher amount of rock fragments of metamorphic and sedimentary origin is observed which originate most probably from the low-grade metamorphic mostly Neoproterozoic basement. The positive correlation of Ti, Y, U, and Zr in the Late Permian to Triassic samples underlines the presence of ultra-stable heavy minerals like zircon and rutile. Furthermore, high maturity and enrichment of zircon is mirrored by high Si content and Th/Sc as well as Zr/Sc ratios (Fig. 7B). Moreover, several samples show a strong depletion of mobile trace elements including Zn. This requires efficient chemical

335 weathering in case of first cycle sediments (McLennan et al., 1993; Avigad et al., 2005) and/or recycling of mature sediments

336 or alternatively long-distance transport. Around the PTB the geochemical signatures including REE patterns are less consistent

337 among different samples than for the other time intervals and show several outliers.

338 Middle to Late Triassic sandstones gradually change back to more immature composition, even though the low maturity of the

339 Early Permian is not reached again. Note that the petrographic immaturity is caused by lithoclasts instead of feldspars as in the

340 Early Permian (Fig. 3). Because these lithoclasts are mostly quartz-rich, the total SiO$_2$ content is as high as for the Late Permian

341 to Early Triassic and also the CIA keeps as high as around the PTB. Trace element spectra a more conformable and less erratic.

342 Ultra-stable minerals drop from a maximum of 95 % back to 47 % and garnet becomes the dominating heavy mineral again.

343 Of specific interest is that the relatively unstable metamorphic mineral epidote occurs more frequently in the Upper Triassic

344 and is completely missing in the Early Permian and only rarely found at the Permian-Triassic transition. This points to fresh

345 input from the low-grade metamorphic Neoproterozoic basement.

5.2 Recycling

347 Potential sources for recycling of older sediments are the Enticho Sandstone and the Edaga Arbi Glacials (Lewin et al., 2018).

348 The distribution of these sediments follows a glacially scoured palaeorelief with SW-NE or S-N trending tunnel valleys where

349 maximum thickness occurs (Dawit and Bussert, 2007). Outside of these valleys, the glacial deposits show a patchy distribution.

350 This is the case e.g. for the Fincha section. Nevertheless, it must be assumed that the ice sheet and its deposits had covered the

351 entire region before the Blue Nile Basin began to form in the Early Permian (Bussert and Schrank, 2007). In the Blue Nile

352 Basin area, the older glacial deposits are scarce and much less widespread than in northern Ethiopia, which makes their removal

353 by erosion highly probable.

354 To test this hypothesis of recycling of the older sedimentary rocks we compared our results with the previous studies of Lewin

355 et al. (2018 and 2020), who found distinct differences between the Enticho sandstone and the Edaga Arbi Glacials. The Enticho

356 Sandstone consists of quartzarenites and sub-arkoses. The quartz content reaches 95 % and points to high maturity. These Late

357 Ordovician to Early Silurian sandstones are depleted in Rb, Ba, Sr, and K and are enriched in Th, Zr, Si, Th, U, Nb with a

358 pronounced negative Eu anomaly (Lewin et al., 2018). The heavy mineral spectra of the Enticho Sandstone is dominated by

359 ultra-stable heavy mineral group accompanied by variable amount of garnet and monazite (Lewin et al., 2020). In contrast, the

360 sandstones of the Edaga Arbi Glacials are mostly arkoses to sub-arkoses (Lewin et al., 2018; Fig. 3). Edaga Arbi Glacials are

361 enriched in V, Cr, and HREE with weak Eu anomaly. These sandstones are less mature with a quartz content about 75 % and

362 a higher content of feldspar and rock fragments compared to the Enticho Sandstone. The unstable heavy minerals garnet and

363 apatite dominate the heavy mineral spectra.

364 Petrographic and geochemical parameters show a surprisingly high similarity between the Edaga Arbi Glacials and the Early

365 Permian Fincha Sandstone. Both are immature arkoses and subarkoses with a high feldspar content of up to 26 %. Moreover,

366 heavy mineral spectra are strikingly similar with dominance of garnet and apatite and ZTR indices < 20. The Harker diagram

367   of the major oxide and PCA biplots (Figs. 5 and 8B) confirms this similarity showing the same enrichments in Na, Mg, K, Ca,

368   and Mn element concentrations and a complete overlap in the PCA plot (Fig. 8B).

369   In contrast, Late Permian to Early Triassic sandstones are highly mature quartzarenite with an average quartz content of 85 %

370   similar to the Enticho Sandstone. Unstable minerals decrease from the Late Permian toward the Early Triassic and ultrastable

371   heavy minerals increase with ZTR indices up to 89 %.

372   Middle to Late Triassic sandstones contain a significantly higher amount of metamorphic and (meta) sedimentary rock

373   fragments. However, in the Late Triassic unstable heavy minerals such as garnet and staurolite increase and the ZTR index

374   decreases to 54 %.

375   Geochemically, both Late Permian to Early Triassic and Middle to Late Triassic sandstones show enrichment in Si, Th, U, Ti,

376   REE, and HFSEs and depletion of Na, Mg, K, Ca, Rb, K, Ba, and Sr in the PCA biplot similar to the Enticho sandstone (Fig.

377   8B). However, the Late Triassic sandstones petrographically deviate due to the presence of rock fragments in contrast to the

378   Enticho Sandstone. The same enrichment in element compositions is due to the presence of quartz-rich lithic fragments.

379   According to McLennan et al. (1993), recycling can be demonstrated using the ratio of incompatible Th and compatible Sc as

380   Zr/Sc and Th/Sc plot. In this diagram (Fig. 7B), Early Permian sandstones and Edaga Arbi Glacials first follow the

381   compositional trend of basement rocks and then turn into the recycling trend. These similarities confirm recycling of Edaga

382   Arbi Glacials and proximal redeposition in the Early Permian without modifying the immature character.

383   Zr/Sc and Th/Sc ratios of the Late Permian to Triassic sandstones are high compared to the Early Permian. The petrography,

384   geochemistry, and heavy mineral spectra of Late Permian to Early Triassic sandstones become more similar to the Enticho

385   sandstone which point to ongoing unroofing and erosional removal of the uppermost sedimentary cover composed of Edaga

386   Arbi Glacials. The scatter of samples from the Late Permian to Early Triassic can be explained by a patchy distribution of

387   relict Edaga Arbi Glacials and Enticho Sandstone (likely the major source) and exposed basement in the drainage basins of the

388   Blue Nile Basin at this time. The strong increase of lithic fragments and metamorphic unstable heavy minerals in the Late

389   Triassic can be seen as a continuation of this process with the basement becoming the dominant sediment source.

390   **5.3 Source rocks**

391   ~~Arkosic to subarkosic sandstones need feldspar-rich rocks as primary source.~~ As found for the Early Permian, the high feldspar

392   content is inherited from the underlying Edaga Arbi Glacials. In the Zr/Sc and Th/Sc diagram (Fig. 7B), the recycling trend

393   intersects with the compositional trend half between a basaltic and felsic source and significantly lower as the intersect for the

394   Enticho Sandstone which is close to a felsic source. The higher contribution of mafic rocks in the Edaga Arbi Glacials and

395   hence also the Early Permian sandstones is supported by slightly enriched values for Cr, V, HREE and a weaker Eu anomaly

396   (Lewin et al., 2020). Based on single grain geochemistry, Lewin et al. (2020) could also prove a significant input from

397   metamorphic rocks and came to the conclusion that the Edaga Arbi Glacials originate from the local basement of the Arabian

398   Nubian Shield including southern Ethiopia.

399   In contrast to the mixed and local origin of the Edaga Arbi Glacials, Lewin et al (2018) proposed a far-distance and more felsic

400   source rocks for the highly mature Enticho sandstones. Geochemical indicators are enrichment in Ti, Zr, U, LREE, Nb, and a

401   pronounced negative Eu anomaly. Furthermore, the major oxide and trace elements of the Enticho Sandstone show typical

402   composition of an old differentiated crustal sources. The ZTR index is mostly between 70 and 90 %. Garnet and staurolite

403   demonstrate significant contribution from amphibolite- to granulite-facies metamorphic rocks in particular to the slightly less

404   mature glaciogenic part of the Enticho Sandstone. Altogether, Lewin et al. (2018, 2020) concluded that the Enticho Sandstone

405   originate from recycling of Cambrian-Ordovician super fan sediments with some addition of fresh basement rocks from the

406   Saharan Metacraton or the Arabian Nubian Shield indicated by metamorphic heavy minerals such as garnet and staurolite. The

407   Late Permian to Early Triassic Fincha Sandstone shows similar relative element enrichment like the Enticho Sandstone

408   indicative for felsic source rocks. The intersect in the Zr/Sc and Th/Sc diagram (Fig. 7B) also supports a higher contribution

409   of felsic rocks compared to the Edaga Arbi Glacials. Garnet, staurolite, and chloritoid also prove the contribution from

410   metamorphic rocks. Whereas garnet and staurolite are also present in minor proportions in the Enticho Sandstone, chloritoid

411   is missing. Overall, similarity of Late Permian to Early Triassic sandstones and the Enticho Sandstone is less striking than for

412   the Early Permian and the Edaga Arbi Glacials.

413   The downward tendency of recycling of Paleozoic glacial sediments becomes clearly evident for the Middle to Late Triassic

414   Fincha Sandstone. Although relicts may still have contributed to some extent, the petrographic and geochemical imprint points

415   to fresh sources from the Arabian Nubian Shield. The most supporting evidence are the occurrence metamorphic and

416   sedimentary lithoclasts which cannot originate from recycling of the Enticho Sandstone or the Edaga Arbi Glacials, because

417   both do not show these types of lithoclasts. The higher RZi index for the Triassic sandstones and relatively high proportions

418   of unstable metamorphic minerals such as epidote, chloritoid, and staurolite also point to a higher contribution from

419   metamorphic rocks. This means that in the Triassic new sources became available to supply lithic-rich sands and metamorphic

420   heavy minerals. The best candidate is the low-grade metamorphic basement of the ANS to the west. This is in accordance to

421   expected axial sediment transport directions in the Blue Nile Basin which formed as SE to NW oriented rift basin (Gani et al.,

422   2009). In contrast, paleocurrent indicators of both glacial deposits point to S to N directed transport and hence to other source

423   areas.

5.4 Climate imprint

425   The short-lived Late Ordovician or Hirnantian glaciation covered significant areas of northern Gondwana by a vast ice sheet

426   (Le Heron et al., 2018). Lewin et al. (2018) argue that a large part of the material of the Enticho Sandstone originate from

427   Cambro-Ordovician large fan systems which were exposed to intensive chemical weathering in a corrosive atmosphere and

428   vegetation-free conditions (Squire et al., 2006; Morag et al., 2011; Avigad et al., 2005).

429   The second glaciation phase of Late Paleozoic has influenced Ethiopia by a more local ice sheet. Because Ethiopia was in a

430   low- to mid-palaeolatitude, Bussert and Schrank (2007) assume plateau or mountain-type glaciations related to compressive

431   Hercynian uplift which is well constrained in Saudi Arabia (Husseini, 1992). An alternative cause is thermal uplift before the

432 formation of the Blue Nile Rift Basin as postulated for wide areas of Gondwana by Visser and Praekelt (1996). Immature

433 sandstones with unstable minerals of Edaga Arbi Glacials prove minor chemical weathering typical of a glacial environment

434 accompanied by short transport and insufficient time for temporal storage (Lewin et al., 2020; 2018). Bussert (2014) describe

435 glaciogenic depositional environments ranging from glacifluvial, glacideltaic to glaciolacustrine.

436 In the Early Permian, sedimentary facies of the Fincha Sandstone show an alluvial fan (F1) and low sinuosity braided river

437 system (F2), pointing to a transition from semiarid to humid conditions. Palynoflora investigated by Dawit (2014) reveal a

438 gymnosperm-dominated upland flora in the aftermath of the Permocarboniferous glaciation which becomes more diverse and

439 was mostly adapted to seasonally cool, consistently moist, mire environments. A humid environment with possibly pronounced

440 silicate weathering seems to contradict the immature petrography of Early Permian sandstones found in our study.

441 Nevertheless, taking together the high availability of unconsolidated glaciogenic sediment of the Edaga Arbi Glacials available

442 for erosion, a high topography, cool temperatures, and rapid, short-distance transport in alluvial fan systems and braided rivers

443 can well explain the almost unchanged inheritance of glacial sediment composition in the Early Permian Fincha Sandstone.

444 In the Late Permian to Early Triassic, sediment facies shows lacustrine conditions with gilbert-type deltas (F3). Although

445 sedimentological conditions show no change at the Permian-Triassic boundary and a clear physical unconformity is not

446 recognizable, an abrupt microfloral change is evident within member F3 of the Fincha Sandstone. This change is marked by

447 the extinction of glossopterid and cordaitalean gymnosperms, and by the extreme decline of a range of gymnospermous and

448 pteridophytic palynomorph groups. Dawit (2014) interprets this abrupt microfloral change as the approximate location of the

449 Permian-Triassic boundary in the Blue Nile Basin. Lacustrine conditions and the lack of red-bed development around the PTB

450 as in other parts of Gondwana points to ongoing humid conditions and little climate change in the Blue Nile Basin, but reduced

451 floral diversity. Our compositional data of this part in the Fincha Sandstone shows increasing maturity and gradual

452 disappearance of typical petrographic tracers from recycling of the Edaga Arbi Glacials. As discussed before, this trend can

453 be adequately explained by unroofing. However, lower vegetation cover and possibly more corrosive rain due to volcanic

454 emission of the Siberian Trap volcanism may have enhanced this trend (Benton and Newell, 2014).

455 The middle to late Triassic depositional environments shows multi-story sheet sands in a alluvial plain (F4), a continental

456 lacustrine environment (F5) and an ongoing humid palaeoclimate (Dawit, 2014). Red-beds in the upper Fincha Sandstone (F5)

457 indicate seasonal dry conditions. Palynofloral assemblages comprise more diverse and new species attributable to

458 corystosperm-, conifer-, and ferndominated floras. These florae might have favourably adapted to coastal plain wetland

459 environments. Sandstone composition shows a gradual decrease of maturity in the upper Fincha Sandstone (F5). This may be

460 linked to seasonally drier conditions and again increase of event-based, rapid sediment transport, but further unroofing and

461 change to the metamorphic basement of the ANS is able to explain this trend as well. Again, provenance change and climate

462 act in the same direction and would both enhance the observed compositional trend.

463 To clarify the influence of climate on the maturity and composition of the studied sandstones, we used a combination of the

464 CIA and the WIP as suggested by Garzanti et al. (2013a) (see Fig. 7A). The CIA value may yield an ambiguous picture in

465 settings with intense sediment recycling, in which the calculated CIA may reflect the weathering conditions in the older

466   sedimentary environment rather than the climate condition of the source area (Huntsman-Mapila et al., 2009; Bassis et al.,

467   2016) and the mobile elements Na, K, Mg, and Ca which are used to calculate the CIA may be impacted by quartz dilution.

468   Therefore, Garzanti et al. (2013a) propose to use the CIA/WIP ratio as a proxy to disentangle recycling and weathering, because

469   this ratio is influenced by quartz dilution rather than weathering (Garzanti et al., 2013a; 2013b; 2019).

470   The low CIA value of 59 and high WIP of 47 for the Early Permian indicate low to moderate weathering and survival of mobile

471   alkali and alkaline trace elements. The CIA/WIP ratio of ~ 1.6 prove a low weathering degree under the humid but cold climate

472   for the Early Permian sandstone.

473   The Late Permian to Early Triassic sandstones combine a high average CIA of around 82 with a lower average WIP of around

474   16. The mean CIA/WIP ratios are between 10 and 38. The highest value for CIA and the lowest for WIP is seen for the

475   quartzose interval of the Early Triassic, i.e. after the Permian Triassic boundary. The data of this interval follow the weathering

476   trend. Strong weathering may be also the reason for a more pronounced negative Eu anomaly due to removal of Eu bearing

477   feldspar and the absence of apatite and garnet in the Early Triassic.

478   For the Middle to Late Triassic sandstones, the average CIA value is similarly high as in the Late Permian to Early Triassic

479   sandstones, which are about 87 and 97, respectively. The average WIP is ~ 12 and the average CIA/WIP 17. The high CIA for

480   the Middle to Late Triassic sandstone is caused by a high amount of quartz-rich rock fragments, whereas unstable heavy

481   minerals such as garnet, epidote, and chloritoid reappear. Hence, in the Late Triassic the CIA seems to be more controlled by

482   a change of provenance than by a changing weathering regime. In summary, the climatic imprint on the composition of the

483   Fincha Sandstone is minor compared to recycling and provenance change. In the Blue Nile Basin the climate remains relatively

484   humid over the entire Permian to Triassic with some changes in seasonality. Despite this relative persistence, climatic indices

485   show strong changes which can be well explained by changes in recycling and provenance during the rifting of the Blue Nile

486   Basin. Nevertheless, around the Permian Triassic boundary a strong shift in CIA, ZTR and maturity is observed, which might

487   be linked to more corrosive atmospheric conditions as proposed by several authors (for review see Benton and Newell, 2014).

488   Super-mature character of the Early Triassic sandstones of has been also reported by Wopfner (1989, 1994) in Tanzania, which

489   he interprets as a product of the intensive chemical weathering of the source rocks and a vast quartz supply by high water

490   influx into the depositional environments (Wopfner, 1989).

5.5 Palaeogeographic and temporal scenario

492   By considering all the results from petrography, geochemistry, heavy mineral spectra and comparison with the Edaga Arbi

493   Glacials and Enticho Sandstone, we propose a scenario for the evolution of the Fincha Sandstone in the Blue Nile Basin as a

494   schematic model (Fig. 12). After consolidation of the Pan-African basement in north-eastern Africa in the Neoproterozoic, a

495   broad peneplain was developed in the Cambrian that was covered by a large continental ice sheet in the Upper Ordovician (e.g.

496   Dawit, 2010; Ghienne et al., 2007; Le Heron and Craig, 2008). Until the successive Permo-Carboniferous glaciation no

497   sedimentary record exists in Ethiopia. The glacial erosion caused deposition of the glaciogenic Enticho Sandstone during the

498   Late Ordovician-Early Silurian and Edaga Arbi Glacials in the Late Carboniferous-Early Permian, preferentially by filling of

499 tunnel valleys or thinner and discontinuous deposits outside (Bussert, 2014). After the glacial periods, the Blue Nile Basin was

500 formed in the first phase of Karoo rifting from the Late Carboniferous onward (Gani et al., 2009, Fig. 12A). During the Early

501
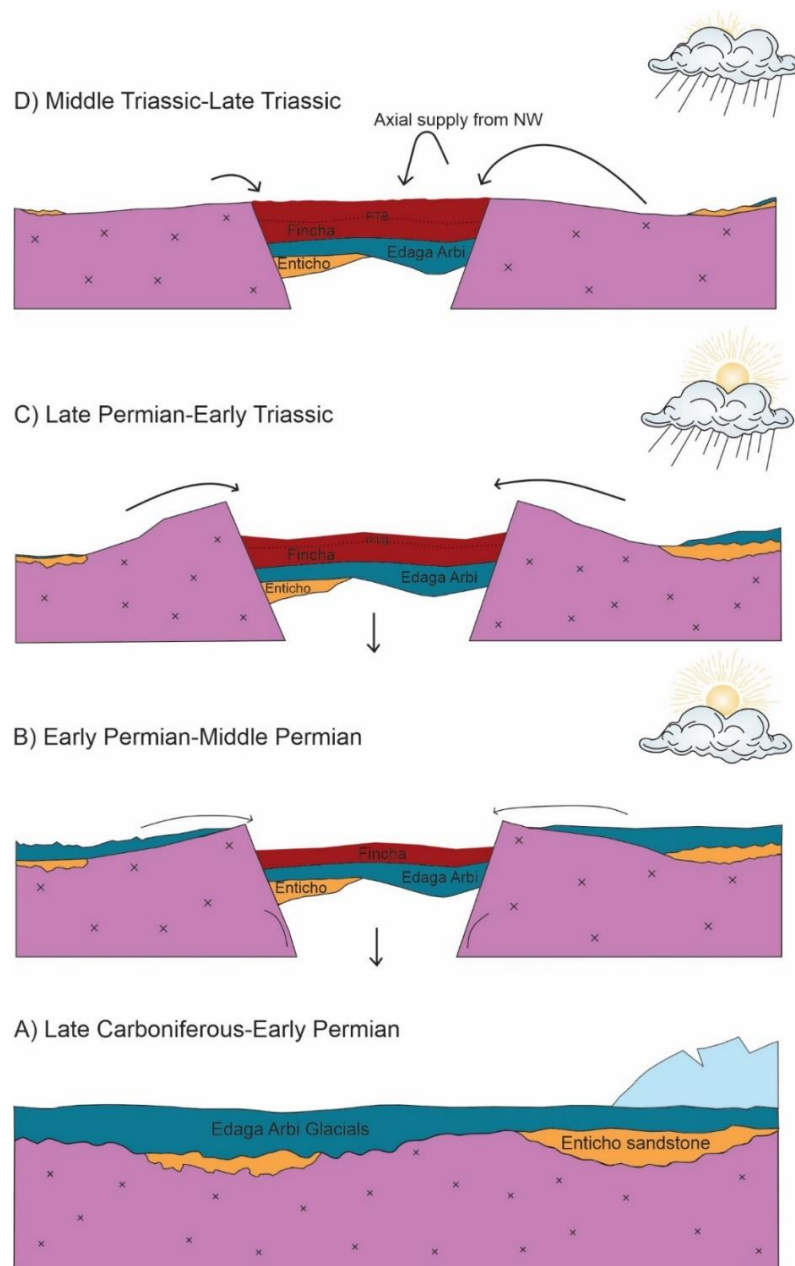
502 **Figure. 12:** Schematic model for the possible scenario of the Fincha Sandstone evolution during the Late Palaeozoic to Early Mesozoic.

503 to Middle Permian, the lower Fincha Sandstone was deposited in the rift valley. According to our results this happened by

504 reworking of significant volumes of the Edaga Arbi Glacials under a semiarid to humid climate (Fig. 12B). Erosion and uplift

505 of the rift shoulders continued throughout the Permian-Triassic transition. The much higher maturity of the middle Fincha
506 Sandstone can be explained by a combination of recycling of the quartzose Enticho Sandstone after removal of the Edaga Arbi
507 Glacials and strong chemical weathering (Fig. 12C). The very high value of CIA/WIP ratio with negative Eu anomaly of the
508 Early Triassic sandstone and also removal of unstable minerals sustain this hypothesis that the sediments suffered from
509 intensive chemical weathering and recycling.

510 By the Middle to Late Triassic, also the Enticho Sandstone had been largely removed, and the metamorphic basement
511 increasingly contributed to sediment generation and sediment supply (Fig. 12D). Metamorphic and sedimentary lithic
512 fragments point to contributions also from low-grade metamorphic terrains which are more widely distributed in the northwest
513 and make a stronger role of axial sediment transport through the rift probable. This is further evidenced by reoccurrence of
514 unstable metamorphic heavy minerals such as garnet, staurolite and epidote as well as relatively high proportions of
515 metamorphic and (meta-)sedimentary lithoclasts. Feldspar remains subordinated which appears to be a consequence of low
516 feldspar fertility of the low-grade metamorphic source rocks rather than strong chemical weathering. Nevertheless, the virtual
517 absence of apatite in contrast to the Early Permian can be taken as argument that chemical weathering intensity was still high
518 in the Middle and Late Triassic. This fits to palynological and facies interpretations of Dawit (2014).

519 **6 Conclusions**

520 The Fincha Sandstone is the initial deposit of the Blue River Basin after Karoo-rifting started around the Permo-Carboniferous
521 boundary. Our results from petrography, geochemistry, and heavy mineral analysis illustrate a significant difference between
522 the Early Permian and Late Permian to Late Triassic sandstones. The Early Permian sandstones bear a high proportion of
523 unstable minerals such as feldspar, apatite, and garnet, which points to very little chemical weathering. Their petrographic and
524 geochemical composition is strikingly similar to the underlying Edaga Arbi Glacials so that a large proportion of the lower
525 Fincha Sandstone must originate from recycling. The conservation of the low maturity of the former glacial deposits can be
526 explained by a combination of high erodibility of mud-rich glaciogenic sediments, a high relief, short-distance transport in
527 alluvial fans and braided rivers, and a semiarid to moderately humid climate.

528 In contrast, the Late Permian to Triassic sandstones show a strong gradual increase in maturity. Unstable minerals are strongly
529 reduced and the ZTR index reaches 95 % and the CIA/WIP ratio becomes highest in the entire succession. On the one hand,
530 this can be assigned to recycling of the quartzose glacial Enticho Sandstone which underlies the Edaga Arbi Glacials and would
531 have been increasingly eroded after the removal of the latter (Lewin et al., 2018). However, the similarity is not that close as
532 for the Early Permian and the Edaga Arbi Glacials. In particular, fine-grained lithic fragments are present, and the proportion
533 of zircon is lower, whereas the proportion of rutile and tourmaline is higher compared to the Enticho Sandstone. Hence, a
534 climate contribution is highly probable. Palynological data and lacustrine-deltaic sediment facies prove highly humid
535 conditions. Probably, abnormal weathering conditions with a corrosive atmosphere at the PTB have accentuated the maturity
536 peak in the Fincha Sandstone. In the Middle to Late Triassic, further downcutting into the Southern Arabian Nubian Shield is

537 evident from significant increase of metamorphic heavy minerals such as garnet and epidote together with a relatively high
538 amount of metamorphic and (meta-) sedimentary lithoclasts (ca. 10 to 45 %). The latter are rare in both glacial formations
539 which were supplied from the south (Bussert, 2010; Lewin et al., 2020). These lithoclasts are typical for low- to medium grade
540 metamorphic terrains which are widespread to the northwest of the study area and point to axial sediment supply along the
541 Blue Nile rift direction. Because of their quartzose nature this trend is less obvious in the geochemical data.

542 In summary, the Fincha Sandstone archives the successive erosion of East Africa during formation of Karoo-equivalent
543 extensional basins, first dominated by recycling of platform sediments, and since the Middle Triassic dominated by basement
544 erosion. Climate imprint is mirrored by conservation and/or shift of petrographic and geochemical parameters from platform
545 sediments. These parameters indicate semiarid conditions in the Permian, whereas the climate became humid around the PTB.
546 The higher humidity persisted over the Triassic, however, our parameters make a maximum humidity and maximum chemical
547 weathering around the PTB and in the Early Triassic very probable.

548 **7 Data availability**

549 The corresponding author will provide the all raw data used in this article by upon request.

550 **8 Author contributions**

551 MH, AL, and EL.D organised the field campaign; MM performed the measurements and analysed the data; MH and LS
552 supervised the measurements and data analyses; MM wrote the manuscript draft; LS, MH, AL, and EL.D reviewed and edited
553 the manuscript.

554 **9 Competing interests**

555 We declare that there is no conflict of interest.

556 **10 Acknowledgement**

557 We would express our special thanks to funding by the German Research Foundation (grants DFG 643/643/13-1 and ME
558 3882/4-1). Also, we would acknowledge Guido Meinhold and Robert Bussert for their constructive discussions.

559 **11 References**

560 Andò, S.: Gravimetric Separation of Heavy Minerals in Sediments and Rocks, Minerals., 10(3), 273,
561 https://doi.org/10.3390/min10030273, 2020.

562 Avigad, D., Sandler, A., Kolodner, K., Stern, R.J., McWilliams, M., Miller, N., Beyth, M.: Mass-production of Cambro–
563 Ordovician quartz-rich sandstone as a consequence of chemical weathering of Pan-African terranes: Environmental
564 implications, EARTH & PLANET. SCI. LETT., 240, 818-826, https://doi.org/10.1016/j.epsl.2005.09.021, 2005.

565 Bassis, A., Hinderer, M., Meinhold, G.: Petrography and geochemistry of Palaeozoic quartz-rich sandstones from Saudi
566 Arabia: implications for provenance and chemostratigraphy, Arab. J. Geosci., 9, 400, https://doi.org/10.1007/s12517-016-
567 2412-z, 2016.

568 Bauluz, B., Mayayo, M.J., Fernandez-Nieto, C., Lopez, J.M.G.: Geochemistry of Precambrian and Paleozoic siliciclastic rocks
569 from the Iberian Range (NE Spain): implications for source-area weathering, sorting, provenance, and tectonic setting, Chem.
570 Geol., 168, 135–150, https://doi.org/10.1016/S0009-2541(00)00192-3, 2000.

571 Benton, M. J.: When Life Nearly Died. The Greatest Mass Extinction of All Time, Thames & Hudson, London., 336 pp, 2003.

572 Benton, M.J., Newell, A.J.: Impacts of global warming on Permo-Triassic terrestrial ecosystems, Gondwana Res., 25, 1308-
573 1337, https://doi.org/10.1016/j.gr.2012.12.010, 2004.

574 Bussert, R.: Exhumed erosional landforms of the Late Palaeozoic glaciation in northern Ethiopia: indicators of ice-flow
575 direction, palaeolandscape and regional ice dynamics, Gondwana Res., 18, 356 – 369,
576 https://doi.org/10.1016/j.gr.2009.10.009, 2010.

577 Bussert, R.: Depositional environments during the Late Palaeozoic ice age (LPIA) in northern Ethiopia, NE Africa, J. African
578 Earth Sci., 99, 386–407, https://doi.org/10.1016/j.jafrearsci.2014.04.005, 2014.

579 Bussert, R., Dawit, E.L.: Unexpected diversity: new results on the stratigraphy and sedimentology of Palaeozoic and Mesozoic
580 siliciclastic sediments in Northern Ethiopia, Zentralblatt für Geologie und Paläontologie., Teil I (3/4), 181–198, 2009.

581 Bussert, R., Schrank, E.: Palynological evidence for a latest Carboniferous-Early Permian glaciation in Northern Ethiopia, J.
582 African Earth Sci., 49, 201–210, https://doi.org/10.1016/j.jafrearsci.2007.09.003, 2007.

583 Cannon, R.T., Simiyu Siambi, W.M.N., and Karanja, F.M.: The proto-Indian ocean and a probable Palaeozoic Mesozoic
584 triradial rift system in East Africa, Earth Planet. Sci. Lett., 52, 419 – 426, https://doi.org/10.1016/0012-821X(81)90194-1,
585 1981.

586 Corfu, F., Hanchar, J.M., Hoski, P.W., Kinny, P.: Atlas of zircon textures. Reviews in mineralogy and geochemistry, 53(1),
587 469 - 500, https://doi.org/10.2113/0530469, 2003.

588 Chorowicz J.: The East African rift system, J. Afr. Earth Sc., 43, 379–410, https://doi.org/10.1016/j.jafrearsci.2005.07.019,
589 2005.

590 Dawit, E.L.: Adigrat Sandstone in Northern and Central Ethiopia: Stratigraphy, Facies, Depositional Environments and
591 Palynology, Ph.D. thesis, University of Berlin, Germany, 166 pp., 2010.

592 Dawit, E. L.: Permian and Triassic microfloral assemblages from the Blue Nile Basin, central Ethiopia, J. African Earth
593 Sci., 99, 408-426, https://doi.org/10.1016/j.jafrearsci.2014.04.011, 2014.

594 Dawit, E.L., and Bussert, R.: Stratigraphy and Facies Architecture of Adigrat Sandstone, Blue Nile Basin - Central Ethiopia,
595 Zbl. Geol. Paläont. Teil I., 3/4, 217-232, 2007.

596 Dickinson, W.R.: Interpreting detrital modes of greywacke and arkose, J. Sediment. Res., 40, 695–707,
597 https://doi.org/10.1306/74D72018-2B21-11D7-8648000102C1865D, 1970.

598 Dudás, F.Ö., Yuan, D., Shen, S., Bowring, S.A.: A conodont-based revision of the 87Sr/86Sr seawater curve across the
599 Permian-Triassic boundary, Palaeogeogr. Palaeoclimatol. Palaeoecol., 470, 40-53,
600 https://doi.org/10.1016/j.palaeo.2017.01.007, 2017.

601 Erwin, D.H.: The Permo–Triassic extinction, Nature., 367, 231–236, https://doi.org/10.1038/367231a0, 1994.

602 Erwin, D.H.: How Life on Earth Nearly Ended 250 Million Years Ago, Princeton University Press, Princeton., 306 pp, 2006.

603 Fairbridge, R.W.: The fracturing of Gondwanaland, in: The Ocean Floor, edited by: Scrutton, R.A., and Talwani, M.,
604 Chichester, John Wiley and Sons, 229–23, 1982.

605 Fielding, C. R., Frank, T. D., Tevyaw, A. P., Savatic, K., Vajda, V., McLoughlin, S., Mays, C., Nicoll, R.S., Bocking, M.,
606 Crowley, J.L.: Sedimentology of the continental end-Permian extinction event in the Sydney Basin, eastern
607 Australia, Sedimentology., 68, 30-62, https://doi.org/10.1111/sed.12782, 2020.

608 Flores, G.: The Cretaceous and Tertiary sedimentary basin of the African coasts, Pt 2. South and east coast, Paris, Assoc,
609 African Geol. Surv., 81, 111 pp, 1973.

610 Folk, R. L.: Petrography of sedimentary rocks, Austin, Tex., Hemphill's Bookstore, 170 p, 1968.

611 Galehouse, J.S.: Point counting, in: Procedures in sedimentary petrology, edited by: Carver, R. E., Wiley, New York, 385-407,
612 1971.

613 Gani, N. D., Abdelsalam, M. G.: Remote sensing analysis of the Gorge of the Nile, Ethiopia with special emphasis on Dejen–
614 Gohtsion region, J. African Earth Sci., 44, 135–150, 10.1016/j.jafrearsci.2005.10.007, 2006.

615 Gani, N. D., Abdelsalam, M. G., Mazzarini, F., Abebe, T., Pecskay, Z, Gani, M. R.: Blue Nile incision on the Ethiopian
616 Plateau: Pulsed plateau growth, Pliocene uplift, and hominin evolution, GSA Today., 17, 4–11,
617 http://dx.doi.org/10.1130/GSAT01709A.1, 2007.

618 Gani, N. D., Abdelsalam, M. G., Gera, S., and Gani, M. R.: Stratigraphic and structural evolution of the Blue Nile Basin,
619 northwestern Ethiopian plateau, Geol J, 44(1), 30-56, https://doi.org/10.1002/gj.1127, 2009.

620 Gärtner, A., Linnemann, U., Sagawe, A., Hofmann, M., Ullrich, B., Kleber, A.: Morphology of zircon crystal grains in
621 sediments – characteristics, classifications, definitions, Geologica Saxonica, Cent. Eur. Geol., 59. 65-73, 2013.

622 Garzanti, E., and Andò, S.: Heavy-mineral concentration in modern sands: implications for provenance interpretation, in:
623 Heavy minerals in use, Developments in Sedimentology Series, edited by: Mange, M., Wright, D., 58. Elsevier, Amsterdam,
624 517–545, 2007.

625 Garzanti, E., Andò, S., and Vezzoli, G.: Grain-size dependence of sediment composition and environmental bias in provenance
626 studies, EARTH & PLANET. SCI. LETT., 277(3-4), 422-432, http://dx.doi.org/10.1016/j.epsl.2008.11.007, 2009.

627 Garzanti, E., Padoan, M., Andò, S., Resentini, A., Vezzoli, G., and Lustrino, M.: Weathering and relative durability of detrital
628 minerals in equatorial climate: sand petrology and geochemistry in the East African Rift, J Geol., 121(6), 547-580,
629 http://dx.doi.org/10.1086/673259, 2013a.

630 Garzanti, E., Vermeesch, P., Andò, S., Vezzoli, G., Valagussa, M., Allen, K., and Al-Juboury, A. I.: Provenance and recycling
631 of Arabian desert sand, Earth-Sci. Rev., 120, 1-19, https://doi.org/10.1016/j.earscirev.2013.01.005, 2013b.

632 Garzanti, E., Vermeesch, P., Vezzoli, G., Andò, S., Botti, E., Limonta, M., Dinis, P., Hahn, A., Baudet, D., De Grave, J., and
633 Yaya, N. K.: Congo River sand and the equatorial quartz factory, Earth-Sci. Rev., 197, 102918,
634 https://doi.org/10.1016/j.earscirev.2019.102918, 2019.

635 George, R., Rogers, N., and Kelley, S.: Earliest magmatism in Ethiopia: evidence for two mantle plumes in one flood basalt
636 province, Geology., 26, 923–926, https://doi.org/10.1130/0091-7613(1998)026%3C0923:EMIEEF%3E2.3.CO;2, 1998.

637 Getaneh, A.: Lithostratigraphy and environment of deposition of the Late Jurassic–Early Cretaceous sequence of the central
638 part of Northwestern Plateau, Ethiopia, Neues Jahrbuch für Geologie und Paläontoogie, Abhandlungen., 182, 255–284, 1991.

639 Ghienne, J.-F., Le Heron, D. P., Moreau, J., Denis, M. and Deynoux, M.:. The Late Ordovician glacial sedimentary system of
640 the North Gondwana platform, in: Glacial Sedimentary Processes and Products, International Association of Sedimentologists,
641 edited by: Hambrey, M.J., Christoffersen, P., Glasser, N.F., and Hubbard, B., Special Publications, 39, 295–319, 2007.

642 Hofmann, C., Courtillot, V., Feraud, G., Rochette, P., Yirgu, G., Ketefo, E., and Pik, R.: Timing of the Ethiopian flood basalt
643 event and implications of Plume birth and global change, Nature., 389, 838–841, doi:10.1038/39853, 1997.

644 Huntsman-Mapila, P., Tiercelin, J. J., Benoit, M., Ringrose, S., Diskin, S., Cotten, J., and Hémond, C.: Sediment geochemistry
645 and tectonic setting: Application of discrimination diagrams to early stages of intracontinental rift evolution, with examples
646 from the Okavango and Southern Tanganyika rift basins, J. African Earth Sci., 53(1-2), 33-44,
647 https://doi.org/10.1016/j.jafrearsci.2008.07.005, 2009.

648 Husseini, M.I.: Upper Palaeozoic tectono-sedimentary evolution of the Arabian and adjoining plates, Geol. Soc. Lond. Mem.,
649 149, 419–429, https://doi.org/10.1144/gsjgs.149.3.0419, 1992

650 Ingersoll, R.V., Bullard, T.F., Ford, R.L., Grimm, J.P., Pickle, J.D., and Sares, S.W.: The effect of grain size on detrital modes:
651 a test of the Gazzi-Dickinson point-counting method, J. Sediment. Petrol. 54., 103–116, https://doi.org/10.1306/212F83B9-
652 2B24-11D7-8648000102C1865D, 1984.

653 Jepsen, D. H. and Athearn, M. J.: Geologic plan and section of the left bank of the Blue Nile canyon near crossing of Addis
654 Ababa-Debre Markos road, U.S. Dept. Interior, Addis Ababa: Ethiopia's Water Res, Dept, 1961.

655 Johnson, P. R., Andresen, A., Collins, A.S., Fowler, A.R., Fritz, H., Ghebreab, W., Kusky, T., and Stern, R.J.: Late
656 Cryogenian–Ediacaran history of the Arabian–Nubian Shield: a review of depositional, plutonic, structural, and tectonic events
657 in the closing stages of the northern East African Orogen, J. African Earth Sci., 61, 167–232,
658 https://doi.org/10.1016/j.jafrearsci.2011.07.003, 2011.

659 Kazmin, V.: Explanation of the Geological Map of Ethiopia. Ethiopian Geol. Surv. Bull. 1, 1–14, 1975.

660 Kieffer, B., Arndt, N., Lapierre, H., Bastien, F., Bosch, D., Pecher, A., Yirgu, G., Ayalew, D., Weis, D., Jerram, D.A., Keller,
661 F., and Meugniot, C.: Flood and shield basalts from Ethiopia: magmas from the African Superswell, J Petrol., 45: 793–834,
662 https://doi.org/10.1093/petrology/egg112, 2004.

663 Korte, C., Kozur, H.W., Bruckschen, P,. and Veizer, J.: Strontium isotope evolution of Late 937 Permian and Triassic seawater,

664 Geochim Cosmochim Ac., 67(1), 47–62, https://doi.org/10.1016/S0016-7037(02)01035-9, 2003.

665 Kozur, H.W., and Weems, R.E.: The biostratigraphic importance of conchostracans in the continental Triassic of the northern

666 hemisphere, Geol. Soc., 334, 315–417, http://dx.doi.org/10.1144/SP334.13, 2010.

667 Kumpulainen, R. A.: The Ordovician Glaciation in Eritrea and Ethiopia, NE Africa, in: Glacial Sedimentary Processes and

668 Products, edited by Montanez, I., Hambrey, M. J., Christoffersen, P., N.F. Glasser, N.F., and Hubbard, B.,

669 https://doi.org/10.1002/9781444304435.ch18, 2007.

670 Le Heron, D. P. and Craig, J.: First-order reconstructions of a Late Ordovician Saharan ice sheet, Journal of the Geological

671 Society, London., 165, 19–29, https://doi.org/10.1144/0016-76492007-002, 2008.

672 Le Heron, D. P., Tofaif, S., and Melvin, J.: The Early Palaeozoic glacial deposits of Gondwana: overview, chronology and

673 controversies, in: Past Glacial Environments, edited by: Menzies, J., van der Meer, J. J. M. Elsevier., Amsterdam, 47–73, 2018.

674 Lewin, A., Meinhold, G., Hinderer, M., Dawit, E. L., and Bussert, R.: Provenance of sandstones in Ethiopia during Late

675 Ordovician and Carboniferous–Permian Gondwana glaciations: petrography and geochemistry of the Enticho Sandstone and

676 the Edaga Arbi Glacials, Sediment. Geol., 375, 188-202, https://doi.org/10.1016/j.sedgeo.2017.10.006, 2018.

677 Lewin, A., Meinhold, G., Hinderer, M., Dawit, E. L., Bussert, R., and Lünsdorf, N. K.: Heavy minerals as provenance indicator

678 in glaciogenic successions: an example from the Palaeozoic of Ethiopia, J. African Earth Sci., 165, 103813,

679 https://doi.org/10.1016/j.jafrearsci.2020.103813, 2020.

680 Mansouri, M., and Hinderer, M.: Towards a sediment budget of Permo-Triassic successions in the Central European Basin –

681 Implications for terrestrial perturbations around the Permian-Triassic Boundary (PTB), ZDGG., 172 (4), 565-590,

682 https://doi.org/10.1127/zdgg/2020/0239, 2021.

683 Maruoka, T., Koeberl, C., Hancox, P.J,. and Reimold, W.U.: Sulfur geochemistry across a terrestrial 965 Permian–Triassic

684 boundary section in the Karoo Basin, South Africa, Earth Planet Sc Lett., 206, 101–117, 10.1016/S0012-821X(02)01087-7,

685 2003.

686 Mayne, W.: Review of the Stratigraphy of the Permian-Tertiary Sediments of Madagascar, Petroconsultants, S.A., Geneva, 35

687 pp, 1971.

688 McElhinny, M. W., Embleton, B. J. J., Ma, X. H., and Zhang, Z. K.: Fragmentation of Asia in the Permian, Nature, 293, 212-

689 216 pp, 10.1038/293212a0, 1981.

690 McHargue, T. R., Heidrick, T. L., and Livingston, J. E.: Tectonostratigraphic development of the interior Sudan rifts, Central

691 Africa, Tectonophysics, 213(1-2), 187-202, https://doi.org/10.1016/0040-1951(92)90258-8, 1992.

692 McLennan, S. M., Hemming, S., McDaniel, D. K., and Hanson, G. N.: Geochemical approaches to sedimentation, provenance,

693 and tectonics, Geol. Soc. Am, Special Paper., 284, 21–40, https://doi.org/10.1130/SPE284-p21, 1993.

694 McLennan, S. M.: Rare earth elements in sedimentary rocks: influence of provenance and sedimentary processes, in: Reviews

695 in Mineralogy, edited by: Lipin, B.R., and McKay, G.A., 21, The Mineralogical Society of America, Washington D.C, 169–

696 196 pp, 1989.

697 McLennan, S.M.: Relationships between the trace element composition of sedimentary rocks and upper continental crust,

698 Geochem. Geophys. Geosyst., 2, 1021, https://doi.org/10.1029/2000GC000109, 2001.

699 Mengesha, T., Tadiwos, C., and Workineh, H.: Explanation of the Geological Map of Ethiopia, Scale 1:2,000,000, Ethiopian

700 Institute of Geological Surveys Bull., No. 3, 1996.

701 Morag, N., Avigad, D., Gerdes, A., Belousova, E., and Harlavan, Y.: Detrital zircon Hf isotopic composition indicates long-

702 distance transport of North Gondwana Cambrian- Ordovician sandstones, Geology., 39, 955–958,

703 https://doi.org/10.1130/G32184.1, 2011.

704 Morley, C. K., Ngenoh, D. K., and Ego, J. K.: Introduction to the East African rift system, in: Geoscience of Rift System-

705 Evolution of East Africa, edited by: Morley, C.K., AAPG Studies, 44, 1–18 pp, 1999.

706 Morton, A. C., and Hallsworth, C.: Identifying the provenance-specific features of detrital heavy mineral assemblages in

707 sandstones, Sediment. Geol., 90, 241–256, https://doi.org/10.1016/0037-0738(94)90041-8, 1994.

708 Nesbitt, H.W., and Young, G.M.: Early Proterozoic climates and plate motions inferred from major element chemistry of

709 lutites, Nature., 299, 715–717, http://dx.doi.org/10.1038/299715a0, 1982.

710 Parker, A.: An Index of Weathering for Silicate Rocks, Geol. Mag., 107, 501-504,

711 https://doi.org/10.1017/S0016756800058581, 1970.

712 Powers, M.C: A new roundness scale for sedimentary particles, J. Sediment. Petrol., 23, 117–119,

713 https://doi.org/10.1306/D4269567-2B26-11D7-8648000102C1865D, 1953.

714 Rees, P.M.: Land-plant diversity and the end-Permian mass extinction, Geology., 30(9), 827-830,

715 https://doi.org/10.1130/0091-7613(2002)030%3C0827:LPDATE%3E2.0.CO;2, 2002.

716 Russo, A., Assefa, G., and Atnafu, B.: Sedimentary evolution of the Abbay River (Blue Nile) Basin, Ethiopia, N. Jb. Geol.

717 Paläont. Mh., 5, 291–308, https://doi.org/10.1127/njgpm/1994/1994/291, 1994.

718 SACS: South African Committee for Stratigraphy: Lithostratigraphy of the Republic of South Africa. Part 1: Stratigraphy of

719 South Africa, South West Africa/Namibia and the Republics of Bophuthatswana, Transkei and Venda, in: Handbook

720 Geological Survey of South Africa 8, edited by: L.E. Kent, South Africa, 1980.

721 Salman, I.G., and Abdula, I.: Development of the Mozambique and Ruvuma sedimentary basins, offshore Mozambique,

722 Sediment. Geol., 96, 7-41pp, https://doi.org/10.1016/0037-0738(95)00125-R, 1995.

723 Scotese, C. R., Boucot, A. J., and McKerrow, W. S.: Gondwanan paleogeography and paleoclimatology, J. Afri. Earth Sci.,

724 28, 99–114, https://doi.org/10.1016/S0899-5362(98)00084-0, 1999.

725 Sengor, A.M.C., Lom, N., Zabcı, C., Sunal, G., and Öner, T.: The Saharides: Turkic-type orogeny in Afro-Arabia, Int J Earth

726 Sci., http://dx.doi.org/10.1007/s00531-021-02063-3, 2021.

727 Sephton, M. A., Jiao, D., Engel, M. H., Looy, C.V., and Visscher, H.: Terrestrial acidification during the end-Permian

728 biosphere crisis?, Geology., 43 (2), 159–162, https://doi.org/10.1130/G36227.1, 2015.

729 Sheldon, N. D.: Abrupt chemical weathering increase across the Permian-Triassic boundary, Palaeogeogr. Palaeoclimatol.

730 Palaeoecol., 231, 315–321, https://doi.org/10.1016/j.palaeo.2005.09.001, 2006.

731 Squire, R. J., Campbell, I. H., Allen, C. M. and Wilson, C. J. L. Did the Transgondwanan Supermountain trigger the explosive
732 radiation of animals on Earth?, EARTH & PLANET. SCI. LETT., 250, 116–133, https://doi.org/10. 1016/j.epsl.2006.07.032,
733 2006.

734 Stern, R.J.: Arc assembly and continental collision in the Neoproterozoic East African Orogen: implications for the
735 consolidation of Gondwanaland, Annu Rev Earth Planet Sci., 22, 319–351,
736 https://doi.org/10.1146/annurev.ea.22.050194.001535, 1994.

737 Stern, R. J., Ali, K. A., Abdelsalam, M. G.,Wilde, S. A., and Zhou, Q.: U–Pb zircon geochronology of the eastern part of the
738 Southern Ethiopian Shield, Precambrian Res., 206–207, 159–167, https://doi.org/10.1016/j.precamres.2012.02.008, 2012.

739 Sun, Y., Joachimski, M. M., Wignall, P. B., Yan, C., Chen, Y., Jiang, H., Wang, L. and Lai, X.: Lethally Hot Temperatures
740 During the Early Triassic Greenhouse, AAAS., 338 (6105), 366–370, http://dx.doi.org/10.1126/science.1224126, 2012.

741 Taylor, S. R., and McLennan, S. M.: The Continental Crust: Its Composition and Evolution, Blackwell Scientific Publication,
742 Oxford, UK, 1985.

743 Taylor S. R., and McLennan S. M.: Planetary Crusts: Their Composition and Evolution, Cambridge University Press,
744 Cambridge., 378 pp, 2009.

745 Urung, R., Haranczyk, C., and Chocyk-Jaminska, M.: Easternmost Avalonian and Armorican– Caledonian terranes of Central
746 Europe and Caledonian–Variscan evolution of the polydeformed Krakow mobile belt: geological constraints, Tectonophysics.,
747 302, 133–157, https://doi.org/10.1016/S0040-1951(98)00278-9, 1999.

748 Veevers, J. J., and Powell, C. M. A. (eds.).: Permian–Triassic Pangean basins and foldbelts along the Panthalassan margin of
749 Gondwana, Geol. Soc. Am. Mem., 184, 331–353, https://doi.org/10.1130/MEM184, 1994.

750 Visser, J. N. J., Praekelt, H. E.: Subduction, mega-shear systems and Late Paleozoic basin development of Gondwana, Geol.
751 Rundsch., 86, 632–646, https://doi.org/10.1007/BF02440101, 1996.

752 Wolela, A. M.: Sedimentology, diagenesis and hydrocarbon potential of sandstones in hydrocarbon perspective rift basins
753 (Ethiopia, UK, USA), Ph.D. thesis, The Queen's University, Belfast, 1997.

754 Wolela, A.: Sedimentation of the Triassic–Jurassic Adigrat Sandstone Formation, Blue Nile (Abay) Basin, Ethiopia, J. African
755 Earth Sci., 52, 30-42, https://doi.org/10.1016/j.jafrearsci.2008.04.001, 2008.

756 Wopfner, H.: Palaeoclimate and depositional control of the Karoo sequence in southern Tanzania, Xle Congres International
757 de Stratigraphie et de C-eologie du Carbonifere Baijing 1987, Compte Rendu 4., 89-95, 1989.

758 Wopfner, H.: The Malagasy Rift, a chasm in the Tethyan margin of Gondwana, J. SE-Asian Earth Sci., 9, 451–461,
759 https://doi.org/10.1016/0743-9547%2894%2990056-6, 1994.

760 Wopfner, H.: The Early Permian deglaciation event between East Africa and northwestern Australia, J. African Earth Sci.,
761 29, 77–90, https://doi.org/10.1016/S0899-5362(99)00081-0, 1999.

762 Wopfner, H.: Tectonic and climatic events controlling deposition in Tanzanian Karoo basins, J. Afr. Earth Sci., 34, 167–177,
763 http://dx.doi.org/10.1016/S0899-5362(02)00016-7, 2002.

764   Wopfner, H., Casshyap, S.M.: Transition from freezing to subtropical climates in the Permo-Carboniferous of Afro-Arabia

765   and India, in: Late Glacial and Postglacial Environmental Changes Martini, edited by: I.P., Oxford University Press, Oxford,

766   192–212 pp, 1997.

767   Worku, T., and Astin, T. R.: The Karoo sediments (Late Palaeozoic to Early Jurassic) of the Ogaden Basin, Ethiopia, Sediment.

768   Geol., 76, 7–21, https://doi.org/10.1016/0037-0738(92)90136-F, 1992.

769   Zheng, Q., Cao, C., and Zhang, M.: Sedimentary features of the Permian-Triassic boundary sequence of the Meishan section

770   in Changxing County, Zhejiang Province, Sci. China Earth Sci., 56, 956–969, https://doi.org/10.1007/s11430-013-4602-9,

771   2013.